A parallel GPU-based computational framework for the micromechanical analysis of geotechnical and erosion problems

Zeyd Benseghier, Pablo Cuéllar, Li-Hua Luu, Stéphane Bonelli, Pierre Philippe

Computers and Geotechnics 120 (2020) 103404

Contents lists available at ScienceDirect

Computers and Geotechnics

journal homepage: www.elsevier.com/locate/compgeo

Review

A parallel GPU-based computational framework for the micromechanical analysis of geotechnical and erosion problems

Zeyd Benseghier[a], Pablo Cuéllar[b,*], Li-Hua Luu[a], Stéphane Bonelli[a], Pierre Philippe[a]

[a] Irstea and Aix-Marseille University, 3275 route de Cézanne, 13100 Aix-en-Provence, France
[b] BAM, Federal Institute for Materials Research and Testing, Berlin, Germany

ARTICLE INFO

Keywords:
Offshore geomechanics
Erosion
Micromechanical modelling
LBM-DEM
Parallel computing
GPU

ABSTRACT

This article deals with the relevance and practical feasibility of micromechanical simulations for their application to general geomechanical problems involving fluid-saturated granular assemblies, whether frictional or cohesive. A set of conceptual and numerical tools is here presented, advocating for a parallel computation using graphical processing units (GPUs) to treat large numbers of degrees of freedom with conventional desktop computers. The fluid phase is here simulated with a particle-resolved approach in the frame of the Lattice Botzmann Method (LBM) while the granular solid phase is modelled as a collection of discrete particles from a Molecular Dynamics DEM perspective. The range of possible material behaviours for the solid granular phase is intended here to cover a broad spectrum from purely frictional to viscous cohesive materials with either brittle or transient debonding features. Specific details of the implementation and some validation cases are put forward. Finally, some exemplary applications in the fields of soil erosion and geotechnical profile installation are provided along with a discussion on the parallel performance of the presented models. The results show that a micromechanical approach can be feasible and useful in practice, providing meaningful insights into complex engineering problems like the erosion kinetics of a soil under an impinging jet or the penetration resistance of a deep foundation in a layered soil profile.

1. Introduction

A wide range of large-scale engineering problems involving fluid-saturated granular assemblies (like soils, debris or muds) in interaction with a fluid flow can be characterized by very similar physical mechanisms at the micro-scale. Some examples include for instance the hydraulic failure of superficial soils [1,2], the formation of sand ripples and dunes in riverbeds and deserts [3,4], scouring phenomena for offshore foundations [5,6] or the internal erosion and piping within embankment dams and dikes [7,8]. All these problems can indeed be described micromechanically as systems of soil particles immersed in an ambient fluid whose mechanical action can locally induce particle removal by erosion or fragmentation.

Many of the geotechnical infrastructures potentially endangered by erosion are earthen hydraulic constructions like dams and dykes [8]. In this context, the usual approach for erosion risk assessment is rather macromechanical and mainly empirical based on several ad-hoc erosion tests (see e.g. [9–11]). However, such approaches typically involve the adoption of strong constitutive and hydrodynamic assumptions (e.g. the magnitude of the viscous shear stress at the solid-fluid interface) and are often restricted to the production of empirical correlations between the soil's resistance to erosion and several other soil parameters (e.g. mean grain size, shear strength or plasticity index), which often leads to the estimation of highly variable erodibility parameters depending on the testing method being employed [12]. In this respect, an insight into the microstructural scenarios of particle removal by a fluid would constitute an important step towards clearer relationships between the physical properties of a material and the more application-oriented erodibility parameters. The challenge here is to develop suitable numerical and theoretical tools capable to model at the same time an assembly of discrete solid particles owing mutual frictional and adhesive interactions, the fluid flow within the corresponding pore space, and the complex coupling between the fluid and solid phases.

Concerning the offshore civil constructions, scouring is the main, ubiquitous, form of erosion [13]. Despite the abundant literature on the matter (see e.g. [14,15] and references therein), reliable quantitative predictions of scour for engineering problems are still a difficult challenge. In practice, the scouring assessment often relies on empirical

* Corresponding author.
E-mail addresses: zeyd.benseghier@irstea.fr (Z. Benseghier), pablo.cuellar@bam.de (P. Cuéllar).
URLs: https://www.irstea.fr (Z. Benseghier), https://www.bam.de (P. Cuéllar).

https://doi.org/10.1016/j.compgeo.2019.103404
Received 19 June 2019; Received in revised form 16 December 2019; Accepted 16 December 2019
Available online 10 January 2020

estimations based on scarce monitoring data [16] or small physical model tests in reduced scale [17]. Such experimental tests are usually costly and time-consuming, especially when parameter studies are required, while, in any case, both the general applicability and accuracy of any extrapolations derived from such databases remain open topics.

A more detailed insight into the subject is now starting to emerge from macroscopic numerical simulations involving three-dimensional flow models based on the incompressible Reynolds-averaged Navier–Stokes equations (RANS, see e.g. [18,5]). Such models incorporate for instance the effects of turbulence, vortex-shedding processes and sediment transport (the suspended load). The sea-bed is thereby considered as a single, continuous surface, while its morphological evolution is progressively updated based on a sediment continuity equation and transient estimates of the sediment transport variables. However, this approach also involves strong assumptions at the solid-fluid interface (e.g. a phenomenological erosion law) while the model coefficients often need to be tuned arbitrarily in order to reach a fair agreement of the scour evolution with experimental data. It is in this sense that a micromechanically-based simulation can also provide a new perspective to complement large-scale flow simulations around offshore substructures.

Beyond the erosion phenomena, there is also a broad range of geomechanical problems and geotechnical applications where the fluid-solid interaction at the pore-scale plays a major role for the macro-mechanical behaviour of the whole system. Dramatic examples include for instance the liquefaction of saturated loose deposits during earthquakes [19], the triggering of landslides due to an excess of pore pressure [20] or the global softening of offshore foundations after the occurrence of a severe storm [21,22].

Here, we propose a general computational framework to address local aspects of common engineering issues involving fluid-saturated soils from this particular perspective, i.e. by retaining the focus on the micro-scale phenomena. The approach advocated in this paper combines the algorithmic efficiency of the Discrete Element Method (DEM) for the solid mechanics with the capabilities of the Lattice Boltzmann Method (LBM) for the fluid dynamics.

The LBM is a convenient alternative to other CFD methods (as in [23] or [24]) that retrieves the macroscopic Navier-Stokes hydrodynamic behaviour in the low Mach number limit departing from a microscopic base, i.e. the molecule distribution functions, as in the original Boltzmann equation (see e.g. [25] or [26]). Provided with appropriate coupling methods [27,28], the LBM can reproduce both efficiently and accurately the interaction between a fluid and a system of immersed discrete particles, described themselves by means of a suitable solid mechanics scheme. Such coupling approaches, involving usually a discretization in the LBM an order of magnitude finer than the size of a particle, can be classified as Particle Resolved Simulation schemes (PRS) and contain very few assumptions, often producing high-quality results on the momentum transfer between fluid and solid phases [23]. In contrast, the non-resolved approaches (see e.g. [29]) are generally more efficient from a computational point of view since they involve a much coarser fluid discretization (single fluid cells often up to an order of magnitude larger than the average particle size) but they do require the adoption of additional assumptions to introduce the effects of the solid particles on the fluid flow (see for instance [30] and references therein).

The applications for the LBM-DEM coupled technique are currently growing exponentially (see e.g. [31–33]). Recent developments include for instance coupled simulations of an immersed granular river bed with an order of 10^5 spherical particles as it forms dunes dragged by a river flow [34], the settling of non-spherical and polygonal particles in a viscous fluid [35,36], or the collapse (avalanche) of immersed granular columns [37]. However, the practical use of these techniques has so far been mainly restricted to small-scale academic examples with little direct impact into real-scale civil engineering problems. This is partly due to the extremely high computational cost involved for the discrete simulation of soil at a representative scale (e.g. millions of soil grains interacting with a structure) in combination with the necessary high refinement degree of the fluid mesh in order to fully resolve the flow around the solid particles (around 10–30 fluid divisions per grain diameter depending on the application, see [32]).

However, this practical constraint for the modelling scale and refinement is being progressively overcome by means of high-performance parallel computation (HPC) as in [34]. Some of the key issues to be addressed in this respect are the strategies for domain decomposition, the efficient distribution of data among the multiple processors, the synchronization protocols and the local communication between neighboring processors/domains involving OpenMP (Open Multi-Processing) or MPI (Message Passing Interface) for CPU clusters, see e.g. [38,39]. In this respect, several efficient codes for high-performance LBM and LBM-DEM computations (MPI approach) have been developed in recent years and are available in an open-source basis, including for instance PALABOS (LBM for CPU clusters provided by the Scientific and Parallel Computing group at the University of Geneva), the waLBerla platform [40,41] at the University of Erlangen, and OpenLB developed at the Karlsruhe Institute of Technology [28].

However, nowadays the use of graphical processing units (GPUs) is gaining growing relevance as an alternative (potentially complementary) technology for distributed computing [42]. Since GPUs are essentially parallel (specifically designed and built for multi-threaded computation) and usually incorporate thousands of processors in a single card, the GPU computation provides the possibility of performing a significant degree of HPC on simple desktop computers without the need to resorting to expensive supercomputing clusters [43,44]. The main drawbacks of using GPUs include their limitations in fast on-chip memory and that their access to global memory is usually quite slow. Besides, the technology and strategies for an extension to multi-GPU computations are not yet fully developed, which often limits the applications in terms of size and number of particles to those suitable for a single GPU. Nevertheless, recent studies with both single- and multi-GPU models show that a reasonable level of scalability is nowadays possible (see e.g. [44] or [42] and references therein).

This paper aims to provide a compilation of useful techniques and practical recommendations for an efficient GPU-based implementation of a micromechanical LBM-DEM simulation tool. No claim is raised here for an optimal efficiency or performance. Instead, the focus is placed rather on the simplicity of a single-GPU approach that may permit the analysis of geomechanical and erosion local problems with conventional desktop computers.

The remainder of this paper is organised in the following manner: The first part introduces briefly the theoretical framework of the LBM and DEM techniques with specific details for the fluid boundaries and solid rheology, the latter including useful models for cohesive bonds and transient damage.

The second part addresses some practical aspects of high relevance for an efficient numerical implementation, namely the phase-coupling scheme and the proposed approach for a GPU parallel computation. The validity of the implementation is briefly discussed in terms of classical benchmark cases, namely the drag coefficient of a settling particle as well as the so-called DKT phenomenon (draft-kiss-tumble trajectories) of a pair of grains.

Finally, the third part of the paper illustrates some applications of the numerical model with exemplary cases of soil erosion and geotechnical profile installation in saturated soil deposits. Useful parameters such as the threshold cohesion for an absence of erosion or the soil resistance to driving (SRD) in a layered soil profile are then derived and the parallel performance of the proposed algorithms is discussed.

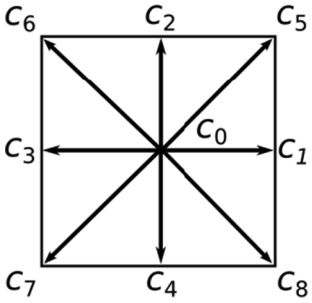

Fig. 1. Set of two-dimensional discrete velocity vectors $\{c_\alpha\}$ for the D2Q9 model of the LBM.

2. Theoretical background

2.1. Particle-resolved fluid model

2.1.1. The Lattice Boltzmann Method

The Lattice Boltzmann Method is a numerical CFD approach that retrieves the Navier-Stokes behaviour of incompressible fluids based on a discretized form of the Boltzmann equation [25]. It involves the definition of a fluid domain discretised as a fixed Eulerian grid (or lattice) of fluid nodes distributed regularly with a spatial distance Δx. A division of the temporal dimension with a constant interval Δt leads to the definition of a complementary discrete velocity space of fluid particles $\{c_\alpha\}$ with the different directions to reach a direct neighbouring node denoted by the index α. We use here a two-dimensional configuration with nine velocity vectors $\{c_\alpha\}$, the so-called D2Q9 model [45] shown in Fig. 1, where the set of discrete velocity vectors is defined as:

$$c_\alpha = \begin{cases} (0,\,0) & \alpha = 0 \\ (1,\,0),\,(0,\,1),\,(-1.0),\,(0,\,-1) & \alpha = 1,\,2,\,3,\,4 \\ (1,\,1),\,(-1,\,1),\,(-1.\,-1),\,(1,\,-1) & \alpha = 5,\,6,\,7,\,8 \end{cases} \tag{1}$$

The discretization of the spatial and temporal domains also implies the definition of a characteristic lattice speed $c = \Delta x/\Delta t$ as well as a speed of sound in the lattice system $c_s = c/\sqrt{3}$.

The LBM then consists in the determination of fluid particle populations $f_\alpha(x,\,t)$, i.e. the probability density distribution of fluid particles at the time t and spatial location x with velocity c_α, by solving the discrete form of the Boltzmann equation (Eq. (2))

$$f_\alpha(x + c_\alpha\Delta t,\,t + \Delta t) = f_\alpha(x,\,t) + \Omega_\alpha \tag{2}$$

which is usually decomposed into the following two sub-steps for the collision and advection of fluid particles (eqs (3) and (4) respectively):

$$f_\alpha^{out}(x,\,t) = f_\alpha(x,\,t) + \Omega_\alpha \tag{3}$$

$$f_\alpha(x + c_\alpha\Delta t,\,t + \Delta t) = f_\alpha^{out}(x,\,t) \tag{4}$$

where $f_\alpha^{out}(x,\,t)$ represents the post-collision density distribution function and Ω_α is the collision operator.

The simplest and most popular collision model is the so-called Bhatnagar-Gross-Krook (BGK), or single-relaxation-time model, where all hydrodynamic moments relax towards the thermodynamic equilibrium with a single relaxation parameter τ [46]. The BGK collision operator can be written as:

$$\Omega_\alpha{}^{BGK} = -\frac{f_\alpha(x,\,t) - f_\alpha^{eq}(x,\,t)}{\tau} \tag{5}$$

where $f_\alpha^{eq}(x,\,t)$ is the distribution function at thermodynamic equilibrium given as a function of the macroscopic quantities for fluid density ρ and velocity $\boldsymbol{u}$:

$$f_\alpha^{eq}(\rho,\,\boldsymbol{u}) = \rho w_\alpha\left(1 + 3c_\alpha{\cdot}\boldsymbol{u} + \frac{9}{2}(c_\alpha{\cdot}\boldsymbol{u})^2 - \frac{3}{2}\boldsymbol{u}{\cdot}\boldsymbol{u}\right) \tag{6}$$

with the single weights w_α taking the following values:

$$w_\alpha = \begin{cases} 4/9 & \alpha = 0 \\ 1/9 & \alpha = 1,\,2,\,3,\,4 \\ 1/36 & \alpha = 5,\,6,\,7,\,8 \end{cases} \tag{7}$$

The macroscopic variables for fluid density and velocity can be obtained from the distribution function as follows:

$$\rho = \sum_{\alpha=0}^{8} f_\alpha \tag{8}$$

$$\boldsymbol{u} = \frac{1}{\rho}\sum_{\alpha=0}^{8} f_\alpha c_\alpha \tag{9}$$

while the fluid pressure is directly given by the following state equation:

$$p = c_s^2\rho \tag{10}$$

On the other hand, the assumed relationship between the relaxation time τ and the kinematic viscosity of the fluid ν is

$$\tau = \frac{3\upsilon}{c\Delta x} + \frac{1}{2} \tag{11}$$

It has been shown that if the density fluctuations are assumed to be negligible, i.e. when $(\rho - \rho_0)/\rho_0 \sim 0$, the LB equation can recover the incompressible Navier-Stokes equations (see e.g. [26]). This means that in order to simulate correctly an incompressible flow and reduce the density fluctuations of the model, the fluid must be kept in the low range of Mach numbers $Ma \ll 1$ (Ma being the ratio of the maximum fluid velocity to the characteristic speed c, usually with a limit value of $Ma < 0.1$ being used by most authors).

However, the BGK collision model presents certain stability issues and does not ensure unconditionally the non-slip condition at the walls. These deficiencies can be overcome by using either the multiple-relaxation-time approach (MRT, see e.g. [47]) or the two-relaxation-time (TRT) as a simpler particular case (see e.g. [48]). In the TRT model, the probability distribution functions are decomposed into positive and negative parts:

$$\begin{aligned} f_\alpha &= f_\alpha^+ + f_\alpha^- \quad f_\alpha^{eq} = f_\alpha^{eq,+} + f_\alpha^{eq,-} \\ f_\alpha^+ &= \tfrac{f_\alpha + f_{\bar\alpha}}{2} \quad f_\alpha^{eq,+} = \tfrac{f_\alpha^{eq} + f_{\bar\alpha}^{eq}}{2} \\ f_\alpha^- &= \tfrac{f_\alpha - f_{\bar\alpha}}{2} \quad f_\alpha^{eq,-} = \tfrac{f_\alpha^{eq} - f_{\bar\alpha}^{eq}}{2} \end{aligned} \tag{12}$$

where $\bar\alpha$ stands for the spatial direction opposite to the direction α (i.e. $c_{\bar\alpha} = -c_\alpha$). This way, the TRT collision operator can be calculated as:

$$\Omega_\alpha{}^{TRT} = -\omega^+(f_\alpha^+(x,\,t) - f_\alpha^{eq,+}(x,\,t)) - \omega^-(f_\alpha^-(x,\,t) - f_\alpha^{eq,-}(x,\,t)) \tag{13}$$

where $\omega^+ = 1/\tau$ and ω^- is an arbitrary constant. The latter is often calculated based on the so-called "magic parameter" $\Lambda = \left(\frac{1}{\omega^+} - \frac{1}{2}\right)\left(\frac{1}{\omega^-} - \frac{1}{2}\right)$ which appears to produce the most stable simulations for values around $\Lambda = 1/4$ [49].

As an alternative, the generalised multi-relaxation-time LB equation, which assumes that the different moments of the distribution function relax towards equilibrium with different rates, can be written as:

$$f_\alpha(x + c_\alpha\Delta t,\,t + \Delta t) = f_\alpha(x,\,t) - M^{-1}S\left[m_\alpha(x,\,t) - m_\alpha^{eq}(x,\,t)\right] \tag{14}$$

where M is the invertible transformation matrix which relates the distribution functions with the vector of fluid moments $m = Mf$, or in matrix form:

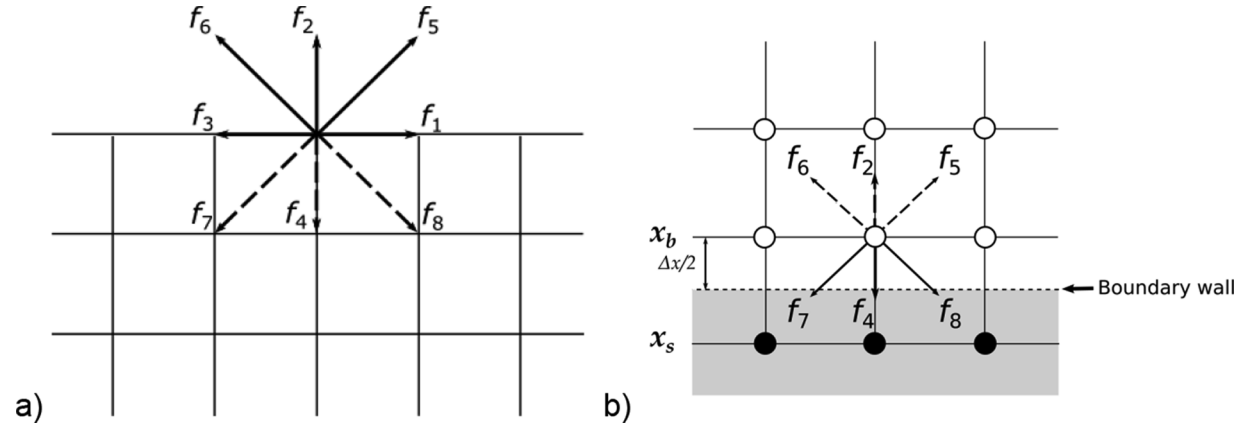

Fig. 2. Boundary conditions in the LBM. (a) Inlet condition located at a northern (upper) boundary, with dashed vectors representing the unknown populations; (b) Half-way bounce-back boundary condition at a southern (bottom) wall, where the boundary wall is assumed to be located right in the middle between solid nodes (solid circles) and fluid nodes (open circles). The grey shaded domain is the solid region and the dashed line corresponds to its boundary. x_b and x_s denote boundary fluid and solid nodes respectively and the dashed arrows represent the reflected distribution functions.

$$\begin{pmatrix} \rho \\ e \\ \epsilon \\ j_x \\ q_x \\ j_y \\ q_y \\ P_{xx} \\ P_{xy} \end{pmatrix} = \begin{pmatrix} 1 & 1 & 1 & 1 & 1 & 1 & 1 & 1 & 1 \\ -4 & -1 & -1 & -1 & -1 & 2 & 2 & 2 & 2 \\ 4 & -2 & -2 & -2 & -2 & 1 & 1 & 1 & 1 \\ 0 & 1 & 0 & -1 & 0 & 1 & -1 & -1 & 1 \\ 0 & -2 & 0 & 2 & 0 & 1 & -1 & -1 & 1 \\ 0 & 0 & 1 & 0 & -1 & 1 & 1 & -1 & -1 \\ 0 & 0 & -2 & 0 & 2 & 1 & 1 & -1 & -1 \\ 0 & 1 & -1 & 1 & -1 & 0 & 0 & 0 & 0 \\ 0 & 0 & 0 & 0 & 0 & 1 & -1 & 1 & -1 \end{pmatrix} \begin{pmatrix} f_0 \\ f_1 \\ f_2 \\ f_3 \\ f_4 \\ f_5 \\ f_6 \\ f_7 \\ f_8 \end{pmatrix} \tag{15}$$

where ρ is the fluid density, e is the energy and ϵ is related to the square of the energy. $j_x = \rho u_x$ and $j_y = \rho u_y$ are respectively the x and y components of the momentum j, P_{xx} and P_{xy} are the diagonal and off-diagonal components of the stress tensor, q_x and q_y are the x and y components of the energy flux, and the vector m^{eq} gathers the equilibrium moments defined as:

$$m^{eq} = \begin{pmatrix} \rho \\ -2\rho + 3(j_x^2 + j_y^2)/\rho \\ \rho - 3(j_x^2 + j_y^2)/\rho \\ j_x \\ -j_x \\ j_y \\ -j_y \\ (j_x^2 - j_y^2)/\rho \\ j_x j_y/\rho \end{pmatrix} \tag{16}$$

Finally, the diagonal relaxation matrix S is defined as $S = diag(0; s_1; s_2; 0; s_4; 0; s_6; s_7; s_8)$. For the D2Q9 model, the coefficients $s_{1,2,4}$ are constants to be chosen in the range $0 < s < 2$ for stability reasons, while $s_7 = s_8 = 1/\tau$. The particular values $s_1 = 1.63$; $s_2 = 1.14$; $s_4 = s_6 = 1.92$ are recommended in [47] and have been used in the following applications.

2.1.2. Boundary conditions

Since both the pressure and velocity fields are only derived variables in the LBM, actually obtained from the particle distribution functions f_α, their respective boundary conditions cannot be imposed directly in a boundary value problem. This means that in the LBM it is necessary to define appropriate rules for the unknown distribution functions at the boundary nodes in order to retrieve the desired values of the hydrodynamic quantities.

Pressure and velocity boundary conditions can for instance be set by using the bounce-back scheme proposed by Zou and He [50], which involves the reflection of the off-equilibrium part of the distribution functions at the boundary. However, the alternative regularized method proposed by Latt and Chopard [51] has been found to be more stable for the prescription of inlet pressure or velocity boundary conditions [52]. This way, the particle populations on the boundary are split into two parts, equilibrium and off-equilibrium, and their values are replaced by the following equation:

$$f_\alpha = f_\alpha^{eq}(\rho, \boldsymbol{u}) + \frac{w_\alpha}{2c_s^4} \boldsymbol{Q_\alpha} : \Pi^{(1)} \tag{17}$$

where $\Pi^{(1)}$ is the first-order stress tensor reconstructed from the known off-equilibrium parts of the particle population $f_\alpha^{neq} = f_\alpha - f_\alpha^{eq}(\rho, \boldsymbol{u})$ and can be written as

$$\boldsymbol{\Pi}^{(1)} = \sum_{\alpha=0}^{8} c_\alpha c_\alpha f_\alpha^{neq} \tag{18}$$

Here, the unknown parts of f_α^{neq} are assigned the values of the known parts in the opposite direction (i.e. $f_{\alpha,unknown}^{neq} = f_{\bar{\alpha}}^{neq}$), and the tensor $\boldsymbol{Q_\alpha}$ is defined as $\boldsymbol{Q_\alpha} = c_\alpha c_\alpha - c_s^2 \boldsymbol{I}$, while the lattice weights w_α have already been introduced above (Eq. (7)).

For the exemplary case of an inlet "northern" boundary (i.e. located at the top, as shown in Fig. 2-a), the tensor $\Pi^{(1)}$ can be reconstructed from the known off-equilibrium populations in the following manner:

$$\begin{aligned} \boldsymbol{\Pi}_{xx}^{(1)} &= f_1^{neq} + f_3^{neq} + 2(f_5^{neq} + f_6^{neq}) \\ \boldsymbol{\Pi}_{yy}^{(1)} &= 2(f_6^{neq} + f_2^{neq} + f_5^{neq}) \\ \boldsymbol{\Pi}_{xy}^{(1)} &= 2(f_5^{neq} - f_6^{neq}) \end{aligned} \tag{19}$$

Alternatively, a much simpler albeit less accurate boundary formulation may be used instead, in which the particle populations are constructed by considering only the equilibrium part (the so-called equilibrium boundary), i.e. by disregarding the second term of the right hand-side in Eq. (17). The advantage of a much easier implementation and straightforward (cheaper) computation may often compensate the slight loss in accuracy as compared to the regularized method.

Finally, the non-slip boundary condition between the fluid and a stationary solid wall can also be imposed by means of the bounce-back scheme. A convenient form of the scheme is the so-called "half-way bounce-back" model, which assumes that the solid wall is located right in the middle between the solid and fluid nodes and has been shown to feature a second-order numerical accuracy [50]. During the streaming step, the wall boundary nodes will reflect any incoming distribution of fluid boundary nodes back into the opposite direction. The explicit scheme of the half-way bounce-back condition is illustrated in Fig. 2-b

and implies the following relationships: $f_5 = f_7; f_2 = f_4; f_6 = f_8$. The general numerical form can be written as:

$$f_{\bar{\alpha}}(\boldsymbol{x_b}, t + \Delta t) = f_{\alpha}^{out}(\boldsymbol{x_b}, t) \tag{20}$$

The implementation of more complex forms of boundary conditions, e.g. periodic BCs for unit representative cells of large/infinite systems or BCs to avoid undesired wall-effects, are out of the scope of this article and have been described elsewhere (see e.g. [53]).

2.2. Solid granular mechanics

Concerning the solid mechanics within the granular phase, significant advances have been made in the past decades on the influence and modelling of different micromechanical features such as particle shape [54], convexity [55] or cohesion [56,57]. However, most of the current DEM models in the recent literature are still lacking versatile interaction models capable of dealing with intergranular cohesion and transient material damage [58], which are key elements that may actually govern the macromechanical failure modes of a whole foundation [59,60]. In this respect, we present here the basic framework of a purely frictional DEM and then introduce an extension of a simple viscoplastic cohesion model [61] that features a subcritical debonding (damage) mechanism based on the work of Silvani et al. [62,63]. This latter property permits the explicit introduction of a characteristic time (i.e. of transience) for the micromechanical debonding process, thus broadening the range of possible material behaviours in the simulations.

2.2.1. Frictional mechanics. The Discrete Element Method

Consistently with the micro-mechanical scope advocated here, the equilibrium of an immersed granular material can be enforced by means of the Discrete Element Method (DEM). The DEM involves the solution of Newton's equations of motion for each of the particles of a granular system in the following fashion [64]:

$$m_i \frac{d^2}{dt^2}\boldsymbol{x}_i = \boldsymbol{F}_i + m_i \boldsymbol{g}; \quad I_i \frac{d}{dt}\boldsymbol{\varpi}_i = \boldsymbol{T}_i \tag{21}$$

where m_i and I_i are the mass and the moment of inertia of the particle i, $\boldsymbol{g}$ represents the acceleration vector due to the body forces acting on the particle (e.g. gravity), while $\boldsymbol{x}_i$ and $\boldsymbol{\omega}_i$ denote its position and angular velocity respectively. $\boldsymbol{F}_i$ and $\boldsymbol{T}_i$ represent the total force and torque acting on the particle, noting that for an immersed particle, the former includes a hydraulic coupling term (see Section 3.1 below) in addition to the intergranular contact forces, i.e. $\boldsymbol{F}_i = \sum_{j \neq i} \boldsymbol{F}_{ij} + \boldsymbol{F}_i^{hydro}$.

The interaction force $\boldsymbol{F}_{ij}$ arising when two neighbouring particles i and j enter in contact (here whenever they overlap) can be decomposed into the usual normal and tangential components F_n and F_s. The normal component F_n can be calculated for instance based on the magnitude of the normal overlap δ_n and assuming a viscoelastic rheology:

$$F_n = \begin{cases} 0 & for \quad \delta_n > 0 \\ -k_n \delta_n - \gamma_n \dot{\delta}_n & for \quad \delta_n < 0 \end{cases} \tag{22}$$

where k_n is the normal contact stiffness and γ_n is the normal viscous damping.

In a similar fashion, the tangential force F_s can also be introduced featuring a viscoelastic-perfectly-plastic rheology accounting for Coulomb's friction limit (i.e. $|F_s| \leq \mu F_n$ with a friction coefficient μ):

$$F_s = -min(\mu F_n, |-k_s \delta_s - \gamma_s \dot{\delta}_s|) sgn(\delta_s) \tag{24}$$

where k_s and γ_s are the contact's tangential stiffness and damping coefficients while δ_s denotes the tangential spring deformation.

As for the conservation of angular momentum in the system, the mechanical torque $\boldsymbol{T}_i$ generated by the tangential force on the particles is complemented by a rolling resistance $\boldsymbol{T}_{ij}^{roll}$ in the following fashion:

$$\boldsymbol{T}_{ij}^{roll} = -\frac{\boldsymbol{v_r}}{|\boldsymbol{v_r}|} \mu_r f_n R_{ij}^{eff} \tag{25}$$

where $\boldsymbol{v_r}$ is the rolling velocity (difference of angular velocities between particles i and j), μ_r is the rolling "frictional" coefficient and R_{ij}^{eff} is the reduced effective radius of the couple defined here as $R_{ij}^{eff} = \frac{r_i r_j}{(r_i + r_j)}$.

Further practical details to ensure the objectivity of the model and the conservation of the total momenta (both translational and angular) can be found for instance in the recent books [65,66].

Concerning the time integration, an algorithm of the velocity-Verlet type can be used to advance both the translational and rotational kinematic variables as follows [67]:

$$\boldsymbol{x_i}(t + \Delta t) = \boldsymbol{x_i}(t) + \boldsymbol{v_i}(t)\Delta t + 1/2\boldsymbol{a_i}(t)\Delta t^2 \tag{26}$$

$$\boldsymbol{\theta_i}(t + \Delta t) = \boldsymbol{\theta_i}(t) + \boldsymbol{\omega_i}(t)\Delta t + 1/2\dot{\boldsymbol{\omega}}_{\boldsymbol{i}}(t)\Delta t^2 \tag{27}$$

The translational and angular velocities are firstly evaluated at a half-time step ($t + 1/2\Delta t$):

$$\boldsymbol{v_i}(t + 1/2\Delta t) = \boldsymbol{v_i}(t) + 1/2\boldsymbol{a_i}(t)\Delta t \tag{28}$$

$$\omega_i(t + 1/2\Delta t) = \omega_i(t) + 1/2\dot{\omega}_i(t)\Delta t \tag{29}$$

while the acceleration is updated according to Newton's equations (Eq. (21)):

$$\boldsymbol{a}_i(t + \Delta t) = \frac{1}{m_i}\boldsymbol{F}_i^{ext}; \quad \dot{\omega}_i(t + \Delta t) = \frac{1}{I_i}\boldsymbol{T}_i^{ext} \tag{30}$$

Finally, the velocities at the time station ($t + \Delta t$) are computed with:

$$\boldsymbol{v}_i(t + \Delta t) = \boldsymbol{v_i}(t + 1/2\Delta t) + 1/2\boldsymbol{a_i}(t + \Delta t)\Delta t \tag{31}$$

$$\omega_i(t + \Delta t) = \omega_i(t + 1/2\Delta t) + 1/2\dot{\omega}_i(t + \Delta t)\Delta t \tag{32}$$

Useful discussions about the choice of rheological parameters, the use of a restitution coefficient and on the critical time step arising from k_n are provided for instance in [68–70].

2.2.2. Solid cohesion

The DEM components introduced so far merely reproduce the mechanics of frictional contacts. This should generally suffice for the analysis of cohesionless geomaterials under gravitational loads or confinement. However, the model can be extended with cohesive interactions to reproduce a broader range of material behaviours with "proper mechanical integrity in the absence of confinement" [61], i.e. allowing for the appearance of tensile normal forces between the particles of the granular material. This kind of behaviour can be very relevant for the mechanical response of various natural granular deposits such as cemented sands (see e.g. [71]).

To this end, a set of solid bonds with a specific rheology can be assumed to exist for any selected group of particles initially at contact. Such bonds can be defined for instance with a linear-elastic-perfectly-plastic rheology characterized by an appropriate set of bond stiffnesses and yield conditions (see e.g. the Bonded Particle Model (BPM) originally proposed by Potyondy & Cundall [72] and later extended to include conductive-convective thermal exchanges in [73]). In this respect, a convenient while realistic bond model with a paraboloidal yield surface in the space of contact forces (a three-dimensional space in terms of F_n, F_s and bending moment M) has been proposed by Delenne and coworkers [61] based on experimental results and is illustrated in Fig. 3. The model assumes that the contact rheology is governed by the bond viscoelastic parameters (e.g. a Kelvin-Voigt model) as long as the interaction forces remain in the interior of the yield surface ζ_u, which is defined in terms of the single thresholds for purely normal, shear and moment failures C_n, C_s and M_b *as:*

$$\zeta_u = \left(\frac{F_n}{C_n}\right) + \left(\frac{F_s}{C_s}\right)^2 + \left(\frac{M}{M_b}\right)^2 - 1 \tag{33}$$

Whenever the contact forces reach or trespass this failure criterion

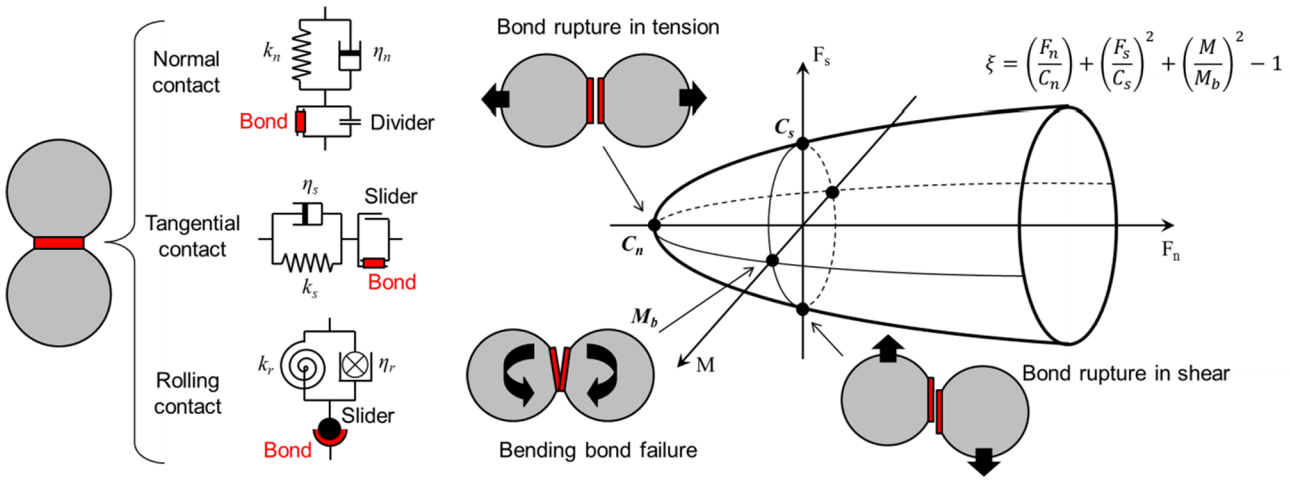

Fig. 3. Left: Rheological model of solid contacts; Right: Yield surface of cohesive bonds in the space of interaction forces, redrawn from [61].

(i.e. when $\zeta_u \geq 0$), the cohesive bond is broken and the contact becomes purely frictional.

Based on the experimental results by Delenne et al [61], the yield thresholds can all be set to depend conveniently on a single parameter C in the following form:

$$C = C_n = 2C_s = \frac{M_b}{2D_{mean}} \tag{34}$$

which thereby represents the strength of the solid bond and fixes the aspect ratios of the paraboloid for different degrees of cohesion. The relative strength of the bonds in a polydisperse assembly can then be characterized by defining a dimensionless number B, ratio of the bond cohesion C to the particle's own buoyant weight, i.e. $B = C/(\Delta\rho g V)$ where $\Delta\rho$ is the submerged apparent density of the solid grains, g is the gravitational acceleration and V is the volume of the particle (for circular particles in a 2D space, a depth-specific volume of $V = \pi D^2/4$ may be used). This dimensionless number is also sometimes called cohesive granular Bond number [74,75]. Preliminary studies indicate that cohesive bonds where $B < 1$ tend to be generally unstable and short-lived (since any slight rearrangement of the assembly under its own weight is likely to cause bond ruptures) while granular assemblies where $B \geq 3$ for all couples appear to remain completely bonded under gravity.

Here it is worth noting that the aspect ratios of the yield surface (Eq. (34)) define the dominant debonding modes of the cohesion model (whether shear, traction or bending failures). This is a useful property that can lead to a great variety of material behaviours, from brittle clustering materials (low M_b ratios) to diffusive decohesion (remote debonding, with low C_s ratios), see [76].

2.2.3. Damage model. Subcritical debonding

The bond model introduced so far may be considered as a "static" cohesion approach due to its lack of transience beyond the binary state-disjunctive, where only intact and fully broken bond states are possible, with sudden state transitions. However, a progressive evolution (or damage) of the cohesive bonds can be introduced for instance by means of the subcritical debonding concept (see e.g. [62,63]) which involves a characteristic debonding time and permits the possibility of a progressive degradation of the cohesive strength for subcritical evolution within the yield surface.

The transience can generally be introduced into the model by any suitable definition of a damage variable d and its time derivative, for instance as follows:

$$\dot{d} = \frac{\langle \zeta_0(F_n, F_s, M, d) \rangle}{\eta C_0} \tag{35}$$

$$0 \leq d \leq d_c(F_n, F_s, M, d) \leq 1 \tag{36}$$

where $\langle \cdot \rangle$ denotes the MacCauley brackets ($\langle x \rangle = x$ if $x \geq 0$; $\langle x \rangle = 0$ if $x < 0$), η is a characteristic time, C_0 stands for the initial damage threshold under pure tensile forces, $\zeta_0(F_n, F_s, M, d)$ is the damage criterion and d_c is the ultimate value of damage, which depends both on the material and loading parameters [62,63].

The damage surface ζ_0 is here conveniently defined in the interior of the failure surface ζ_u and with the same shape (Fig. 4), i.e.

$$\zeta_0 = \left(\frac{F_n}{C_0}\right) + \left(\frac{F_s}{C_s}\right)^2 + \left(\frac{M}{M_b}\right)^2 - (1 - md) \tag{37}$$

where m is a softening parameter (see the analogous model in [62,63]), which for simplicity has been set to unity in the following applications. The sub-space bounded by the yield and damage surfaces defines thereby the combinations of interaction forces that induce bond damage (domain 2, as shown in Fig. 4), while the bond solicitations contained within the damage surface do not cause any bond degradation (domain 1). Any other solicitations outside the yield surface (domain 3) are assumed to cause an immediate rupture of the cohesive bond, as in the original "static" cohesion model.

Here it can be noted that since both the yield and damage surfaces ζ_u and ζ_0 include now a negative dependency on d, this formulation implies that both surfaces are actually displaced towards the origin as the damage variable grows, thus increasing progressively the susceptibility of the bond to further damage or rupture.

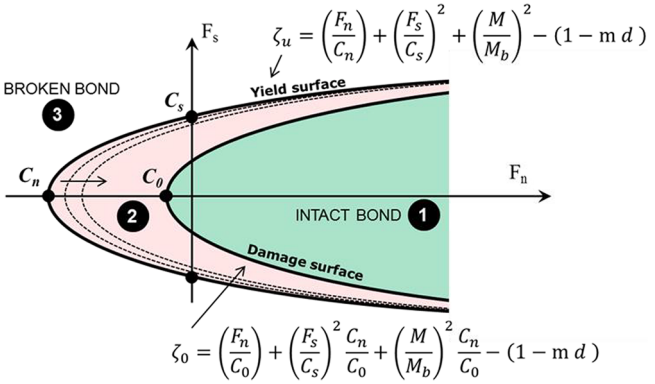

Fig. 4. Damage model for subcritical debonding. Yield and damage surfaces with distinction of solicitation domains for intact cohesive bonds (region 1), evolving damage (region 2) and instant rupture (region 3). For simplicity, the third dimension of bond solicitations (i.e. the rolling moments) has been omitted in the figure.

3. Practical implementation

3.1. Fluid-solid coupling

The phase coupling strategy for the consideration of immersed geomaterials is here based on a juxtaposition of the two separate DEM and LBM models while enforcing the spatial exclusion and a momentum exchange between the phases. The former concerns the temporary conversion of fluid nodes into "solid" nodes for the regions of the lattice covered by the "shadow" of the DEM particles, which are then excluded from the LBM calculations. Conversely, the transition of solid LBM nodes into "uncovered" fluid ones due to the displacement of a moving DEM particle involves the creation of distribution functions for the new fluid nodes (see e.g. Aidun et al. [77], well summarised in Tran et al. [32]).

The microscopic fluid-solid interaction between the two models can then be introduced by means of a suitable momentum-exchange algorithm, for instance by assuming a regularised non-slip bounce-back condition at the solid boundary nodes as proposed by Bouzidi et al. [78]. This approach, which is adapted for the curved moving boundaries of the DEM particles, features a linear interpolation of the post-collision distribution functions involving two fluid nodes x_f and x_{ff} (see Fig. 5-a).

The Bouzidi scheme considers two possible interpolation situations based on the relative distance $q = |x_f - x_\omega|/|x_f - x_s|$ between the boundary fluid and solid nodes, x_f and x_s respectively, and the solid intersection point x_ω:

$$f_{\bar{\alpha}}(x_f, t + \Delta t) = \begin{cases} 2q f_\alpha^{out}(x_f, t) + (1 - 2q) f_\alpha^{out}(x_{ff}, t) + 2\omega_\alpha \rho_\omega \frac{c_{\bar{\alpha}} u_\omega}{{c_s}^2}; & for \quad q < 1/2 \\ \frac{1}{2q} f_\alpha^{out}(x_f, t) + \frac{(2q-1)}{2q} f_\alpha^{out}(x_{ff}, t) + \frac{1}{q}\omega_\alpha \rho_\omega \frac{c_{\bar{\alpha}} u_\omega}{{c_s}^2}; & for \quad q \geq 1/2 \end{cases} \tag{38}$$

where $c_{\bar{\alpha}}$ is the opposite direction of c_α and u_ω is the wall velocity at the intersection point x_ω. This velocity x_ω can be obtained from the particle velocity $\boldsymbol{U}$, the angular velocity of the particle ω and the center of mass of the particle x_c:

$$u_\omega = U + \omega \times (x_\omega - x_c) \tag{39}$$

As a consequence of the particle's translation, some of the solid boundary nodes may convert to fluid nodes, so that the unknown distribution functions must be recovered. Several techniques to solve this issue can be found for instance in [79], where the unknown distributions functions of the fresh fluid nodes are simply approximated using the equilibrium distribution functions $f_\alpha^{eq}(\rho, u_\omega)$. The latter can be computed using the averaged fluid density of the whole system (which generally fluctuates slightly around 1 in lattice units) and the wall velocity at the specified node position just before its conversion to fluid node (see e.g. [80]).

The total coupling force F_i^{hydro} exerted by the fluid on a given particle can then be calculated with the momentum-exchange algorithm [81], i.e. by summation of the momentum exchange between the solid boundary nodes and the fluid nodes:

$$F_i^{hydro} = \sum_{x_f} \sum_{\alpha} [f_\alpha^{out}(x_f, t) + f_{\bar{\alpha}}(x_f, t + \Delta t)] c_\alpha \tag{40}$$

The total torque exerted by the fluid on the solid particle is computed in analogous fashion as

$$T_i^{hydro} = \sum_{x_f} \sum_{\alpha} (x_\omega - x_c) \times [f_\alpha^{out}(x_f, t) + f_{\bar{\alpha}}(x_f, t + \Delta t)] c_\alpha \tag{41}$$

Here it is worth noting that the coupling algorithms based on the momentum-exchange are generally very demanding for a parallel computation, since they involve a frequent memory access to all the neighboring nodes of each boundary node at the perimeter of the particles, thereby reducing the efficiency and speed of parallel computations. In this respect, it may be worth resorting to an alternative method to implement the fluid–solid interaction, e.g. by means of the partially saturated method (PSM) originally proposed by Noble and Torczynski [82]. The PSM merely involves the consideration of a modified non-slip condition of each lattice node based on the solid fraction of a virtual lattice cell associated to it. The virtual lattice cell can thereby be either completely fluid, fully solid or mixed (i.e. partially saturated), as shown in Fig. 5-b. This way, the interaction algorithm avoids the necessity for interpolation with neighboring nodes, hence making its parallelization much more straightforward. In this sense, the PSM appears to be the best alternative for GPU parallel computations.

The PSM is based on the modified BGK equation with the introduction of the solid fraction associated to a given lattice point and a source term to account for the presence of the solid nodes:

$$f_\alpha(x + c_\alpha \Delta t, t + \Delta t) = f_\alpha(x, t) + (1 - B)\Omega_\alpha^{BGK} + B\Omega_\alpha^s \tag{42}$$

where Ω_α^s is the collision operator for solid nodes:

$$\Omega_\alpha^s = [f_{\bar{\alpha}}(\boldsymbol{x}, t) - f_{\bar{\alpha}}^{eq}(\rho, \boldsymbol{u})] - [f_\alpha(\boldsymbol{x}, t) - f_\alpha^{eq}(\rho, \boldsymbol{u_s})] \tag{43}$$

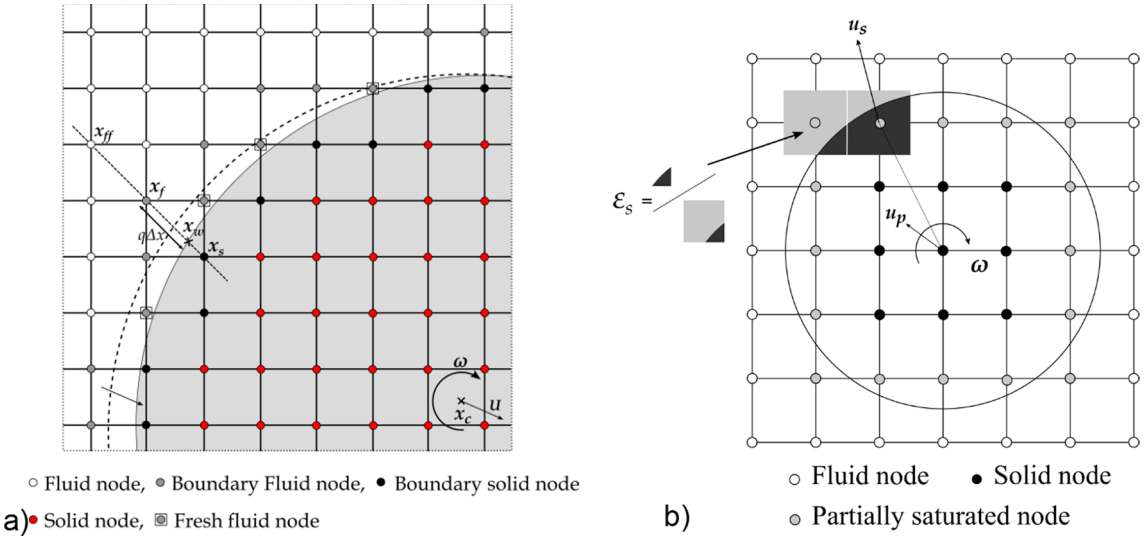

Fig. 5. Modelling concepts for the fluid solid-coupling. (a) Sketch of the fluid-solid boundary around a moving particle in the frame of the momentum-exchange approach, with appearance of new fluid boundary nodes. The dashed line represents the previous position of the particle; (b) Conceptual sketch of the Partial Saturation Method (PSM), redrawn from [53], involving the solid fraction of virtual lattice cells associated to each of the lattice nodes.

where $\boldsymbol{u}$ is the local fluid velocity, $\boldsymbol{u_s} = \boldsymbol{u_p} + \omega \times (\boldsymbol{x} - \boldsymbol{x_c})$ is the velocity of the solid point $\boldsymbol{x}$, and B is a weighting parameter defined in terms of the solid fraction as

$$B = \frac{\varepsilon_s(\tau - 1/2)}{(1 - \varepsilon_s) + (\tau - 1/2)} \tag{44}$$

Here, ε_s represents the solid fraction of the lattice node and is restricted to the range $0 \leq \varepsilon_s \leq 1$, whereby $\varepsilon_s = 0$ corresponds to a lattice node inside a fully fluid virtual cell and $\varepsilon_s = 1$ applies for the case of a lattice node in a fully solid cell. Among the different possible ways to estimate the solid fraction ε_s, a convenient one is to divide the lattice cell with a finer grid and count the number of small sub-cells that are inside the solid particle. This way, the solid fraction can be roughly estimated in 2D as the ratio of solid sub-cells to the surface of the lattice cell.

Then, the force and torque acting on the boundary can be computed as [83]:

$$F = \frac{\Delta x^2}{\Delta t} \sum_{x_n} B(x_n) \sum_{\alpha} \Omega_{\alpha}^{s}(x_n) c_{\alpha} \tag{45}$$

$$T = \frac{\Delta x^2}{\Delta t} \sum_{x_n} B(x_n)(x_n - x_c) \times \sum_{\alpha} \Omega_{\alpha}^{s}(x_n) c_{\alpha} \tag{46}$$

where x_n denotes the lattice nodes which are either partially or fully solid (i.e. all nodes with $\varepsilon_s > 0$) and x_c is the location of the centre of mass of the solid particle.

Finally, and due to the known deficiencies and stability issues of the BGK collision model, we propose here a modified version of the PSM method based on the TRT collision model instead of the BGK one, thereby transforming the equation (42) into:

$$f_{\alpha}(x + c_{\alpha}\Delta t,\ t + \Delta t) = f_{\alpha}(x,\ t) + (1 - B)\Omega_{\alpha}^{TRT} + B\Omega_{\alpha}^{s} \tag{47}$$

Here it is also worth to mention that Zhang et al. [84] have proposed an alternative improvement of the method by using the MRT collision model instead of the BGK, where the collision and streaming steps need to be separated as in the momentum-exchange algorithms (i.e. a Bouzidi-like scheme). However, the implementation proposed here has the advantage that it can be enclosed in one single CUDA-kernel including the calculation step for hydraulic forces (see next section). This way, the overall time performance of our code is improved by a factor of around 2.

For both coupling methods, whether the moment-exchange or the PSM, the total hydraulic force and torque are then introduced into the DEM algorithm (eq. (21)) after conversion to physical units. In addition, the buoyancy effect (i.e. the submerged weight) must also be considered for the DEM particles, for instance by multiplying the gravitational acceleration by the factor $(1 - \rho_f/\rho_s)$.

Concerning the permeability of settled three-dimensional granular samples where all the solid particles are in contact with other particles, a strict geometrical modelling in 2D conditions would lead to the unphysical situation where no fluid paths exist through the contacting network of round particles and thus preclude any permeability. This would also lead in practical terms to the estimation of unrealistic solid fractions for the overlapped lattice nodes at the particle contacts. Therefore, we employ here the so-called hydraulic radius approach (see e.g. [85,86]), by considering that the solid grains have a reduced radius R_h in the LBM domain while keeping the particle's real radius R in the DEM domain. The ratio R_h/R is generally set to values around 0.8, as recommended in [85], while its influence on the simulated drag coefficients and macroscopic permeability are out of the scope of this paper.

With respect to the spatial resolution of the LBM-DEM coupling, we adopt here a fixed minimum resolution of at least 10 lattice nodes per grain dimension (i.e. $\Delta x = D_{min}/10$), as recommended in [87], where D_{min} is the diameter of the smallest particle in the sample.

Another relevant aspect for the solid-fluid coupling relates to the fact that the LBM and DEM often require different time-step sizes for numerical stability, whereby the DEM time-step is usually smaller than the time-step needed for the LBM model. Therefore, an efficient coupling between both methods may include a sub-cycling scheme (higher frequency) for the DEM algorithm. This way the LBM model is only updated once every N_p steps of the DEM algorithm, i.e. the LBM and DEM time-step sizes are here related by the fixed integer ratio N_p. Nevertheless, and in order to minimize the potential loss of accuracy it appears sensible to keep this ratio as low as 2 or 3, if employed at all.

3.2. Computational parallelism for GPUs

In order to take advantage of GPUs to perform heavy and repetitive computational tasks, it is now possible to include so-called CUDA kernels in most modern programming languages. These kernels are called from the CPU (the host) and executed in parallel by the thousands of local micro-processors available in the GPU (the device). It is convenient to devise the kernels for the LBM part so that each thread will perform a specific LBM task at one spatial location in the fluid domain (i.e. one thread for each lattice node) [88]. This way, the two-dimensional LBM domain will be divided into a grid (or patchwork) of two-dimensional CUDA blocks, whereby each block constitutes an array of threads running the same tasks in parallel. The size of the blocks (i.e. the number of parallel threads inside the blocks) is in practice a free parameter within the available capacity of the GPU, which is often limited to $N_{threads,X} \times N_{threads,Y} < 1024$ for most of the current graphic cards. In this respect there is often an optimal value for peak performance, where the block dimensions are commonly chosen as powers of 2 optimizing the GPU's warp size (32 threads).

The total number of blocks is thus controlled by the dimensions of the LBM domain, N_x and N_y respectively in the x and y directions. Here it is also convenient to add an extra block (buffer) in each dimension, just for the case where the LBM domain does not fit exactly in the GPU grid. A return condition is set for all threads in the extra buffer that are not assigned with an actual lattice node, avoiding eventual access to non-declared memory locations. Fig. 6 illustrates a two-dimensional LBM domain divided into blocks of threads and featuring a layer of buffer blocks at the limit of the x dimension.

The LBM's probability distribution functions f_{α} are then stored as a single array in the global GPU memory. For computational efficiency it is very convenient to use here the so-called Structure of Arrays (SoA) format in order to enhance the coalescence of the memory access of the concurrent threads (contiguous memory locations for contiguous threads), see e.g. [88,89] or [90]. This way, the distributions $f_{\alpha}(x_p)$ of a given point x_p with local (LBM) coordinates i and j are actually stored

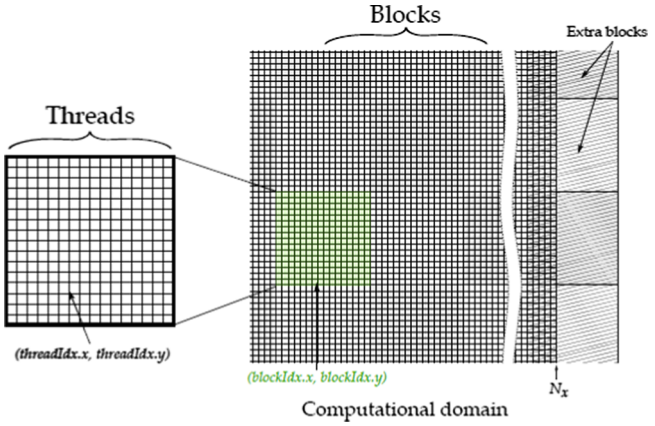

Fig. 6. Decomposition of the computational domain into blocks of threads in CUDA. Each intersection of the grid represents a fluid lattice node (LBM), computed by a single CUDA thread. An additional layer of blocks (buffer) is added for the case where the LBM domain does not fit exactly in the GPU grid.

as $f[i + j{\cdot}N_x + \alpha{\cdot}N_x{\cdot}N_y]$. These locations can then be accessed from the GPU grid in the following manner:

$$i = blockIdx.\,x \times blockDim.\,x + threadIdx.\,x$$
$$j = blockIdx.\,y \times blockDim.\,y + threadIdx.\,y \quad (48)$$

Two separate copies of f can be used to ensure that the data dependency is not violated, namely f_{out} for the post-collision state and f_{in} for the post-streaming distribution. A pseudo-code of the collision and streaming steps with the PSM coupling scheme is summarized in Algorithm 1.

Concerning the solid grains, the DEM kernels can be based on a one-dimensional CUDA grid of grain-threads featuring a fixed number of blocks depending on the total number of particles. Again, the number of threads within the blocks is set to a power of 2 (we use for instance 128) and an extra buffer block is added here as well to ensure that all solid particles are taken into account.

Algorithm 1 (*Pseudo-code of collision and streaming steps for LBM with push and PSM schemes*).

```
Collision and Streaming kernel:
  Get fluid node coordinates i and j from Eq. (48)
  if (i < 0)||(i > N_x − 1)||(j < 0)||(j > N_y − 1) then
    return.
  end if
  Compute macro variables ρ and u from Equations (8) and (9) respectively
  Compute f_α^eq(ρ, u), Eq. (6)
  if ε_s > 0 then
    Get particle's ID
    Get particle's velocity u_s
  end if
  Compute Ω_α^s from Eq. (43)
  Apply the PSM, with either the BGK version (Eq. (42)) or with the TRT scheme (Eq. (47))
  if ε_s > 0 then
    Get particle's ID
    Atomic increment of hydro force and torque acting on the particle (Eqs. (45) and (46) respectively)
  end if
```

With respect to the neighbour search and the contact detection algorithms, we use here a cell-based scheme, where an additional grid of DEM cells covering the whole fluid domain keeps track of the specific particles contained in neighbour cells (see Fig. 7). The cell-size is set here to depend on the maximum grain size R_{max}, for instance as $\Delta x_{DEM} = 2.1{\cdot}R_{max}$, where each cell is likely to contain up to 5 particles, and then the particles are assigned to the cells based on their centre of mass.

The actual distribution of DEM particles in the cell-grid can be generally updated with a reduced frequency depending on the particular study case (here, for instance, every 100 time-steps). This is generally possible if the adopted time-step is small enough and whenever the solid particles don't move excessively (quasi-static problems), avoiding this way the necessity to update the grid too often and thus reducing the computational cost.

To perform the contact detection, first we extract for each particle i its cell-tag (i.e. its actual location in the cell-grid). The contact detection is then performed only within the own and direct neighbouring cells (9 cells in total for 2D conditions) and just for the particles j that have a higher id-number ($i < j$), making use of the reciprocity of the contact interactions ($F_{ji} = -F_{ij}$).

The same procedure can be used for the identification of cohesive bonds in a bonded granular sample, where the particular bond data (i.e. bond state, strength, orientation, etc..) can be stored in the upper part of a symmetric matrix structure with both dimensions equal to the number of particles. For further efficiency, the storage of this highly sparse bond matrix can be done using a compressed format, for instance the Compressed Sparse Column Format (CSC). The idea here is to decompose the sparse matrix (with few non-zero components) into three full arrays with no empty components: A first array "indices" contains the row indices of all non-zero components of the matrix (i.e. the row "address" of the cohesive bond), the second array "data" contains the nonzero values (i.e. the cohesive bond information) and the third array "indptr" contains the array indices within "data" where each column of the sparse matrix starts. This is illustrated exemplarily in Fig. 8 for a group of 11 particles with 8 cohesive bonds. These three arrays need only be constructed during the initial identification of the cohesive bonds (i.e. during the contact detection at time zero).

The pseudo-code for a GPU implementation with CUDA of the LBM-DEM coupling approach presented here is summarized in Algorithm 2 and illustrated as a flowchart in Fig. 9.

Algorithm 2 (*Pseudo-code of GPU implementation for LBM-DEM coupled model*).

```
Main program:
  Declare variables in CPU and any necessary counterparts in GPU
  Initialize variables
  CPU: construct the cohesive bonds data structure (CSC format)
  Copy data from CPU memory to GPU global memory
  DEM kernel: Map solid particles into fluid domain
  DEM kernel: Initialize DEM cell-grid
  for each time-step Δt do
    DEM kernel: Update particle mapping and compute local solid fractions in each cell
    LBM kernel: Perform collision and streaming (Algorithm 1)
    LBM kernel: Enforce boundary conditions
    CPU: Swap f_out and f_in pointers
    if t%100 = 0 then
      DEM kernel: Update DEM cell-grid
    end if
    DEM kernel: Update grain positions and rotations at t + Δt (Eqs. (26) and (27))
        Update linear and angular velocities at t + 1/2Δt (Eqs. (28) and (29))
    DEM kernel: Compute solid contact forces for all particles (i < j) and add the hydro forces
    DEM kernel: Compute linear and angular accelerations at t + Δt (Eq. (30))
    DEM kernel: Correct linear and angular velocities at t + Δt (Eqs. (31) and (32))
    if t%OutFreq = 0 then
      Copy any desired data from the GPU back to the CPU memory
      CPU: visualize results
    end if
  end for
```

3.3. Validation of the numerical code

We now examine the validity of the proposed LBM-DEM coupling technique by means of two classical benchmark problems for micro-mechanical fluid-solid interaction, namely the drag coefficient of a single settling particle for different fluid conditions and the sedimentation trajectories of a pair of interacting grains.

To quantify the hydrodynamic conditions we use here the particle Reynolds number, defined as $Re = v_p D/\nu$ in terms of the terminal settling velocity of the particle in the fluid v_p, the fluid's kinematic viscosity ν and the particle diameter D. In this example, the size of the simulation domain is chosen large enough to minimize the effect of the wall as $N_x \times N_y = 50D \times 80D$, where the particle size D is set to 20 lattice steps Δx. Considering the distance between the lateral boundaries, the wall effects are expected to be negligible, as shown in [91] for domains where $N_x > 100D$.

The particle is initially located at a height $h_0 = 72D$ from the bottom wall. The initial and boundary conditions adopted here are thereby directly comparable to those in [84], with simple bounce-back (non-slip) boundary conditions applied to all walls. The drag coefficient C_D of the two-dimensional particle can then be calculated as

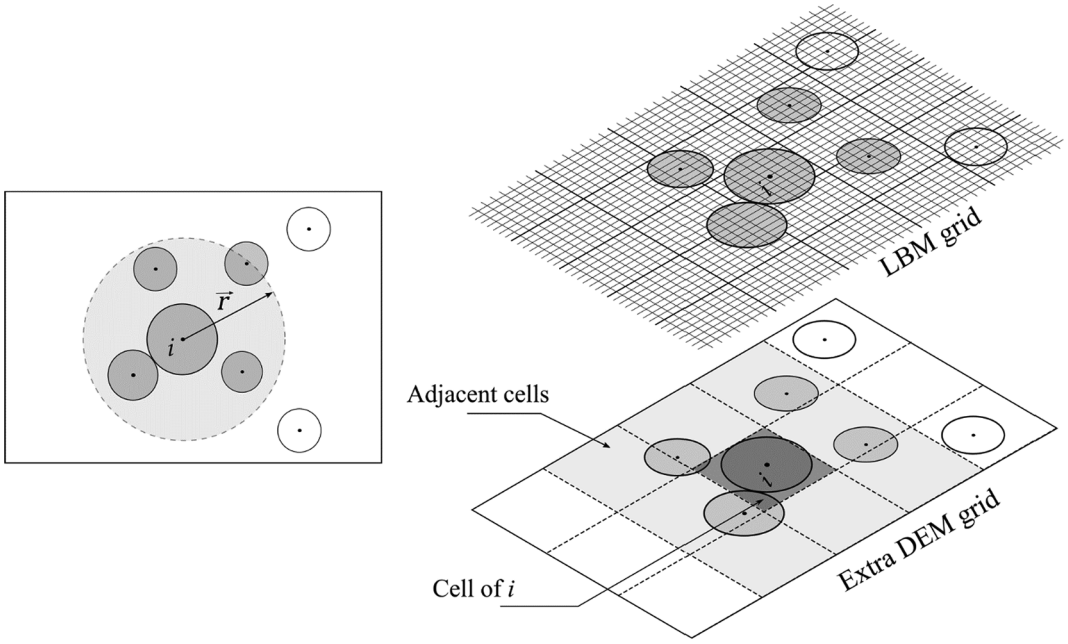

Fig. 7. Alternative paradigms for neighbour search and contact detection. (a) Neighbour lists (e.g. Verlet list) associated to each particle based on a given detection radius (typical of serial or CPU-based codes); (b) Cell-based approach, where the computational domain is divided into an additional cell-grid for the DEM particles with a cell-size of $2.1 \cdot R_{max}$. The possible interactions for a given particle i are only explored for the particles contained in the adjacent (grey) cells.

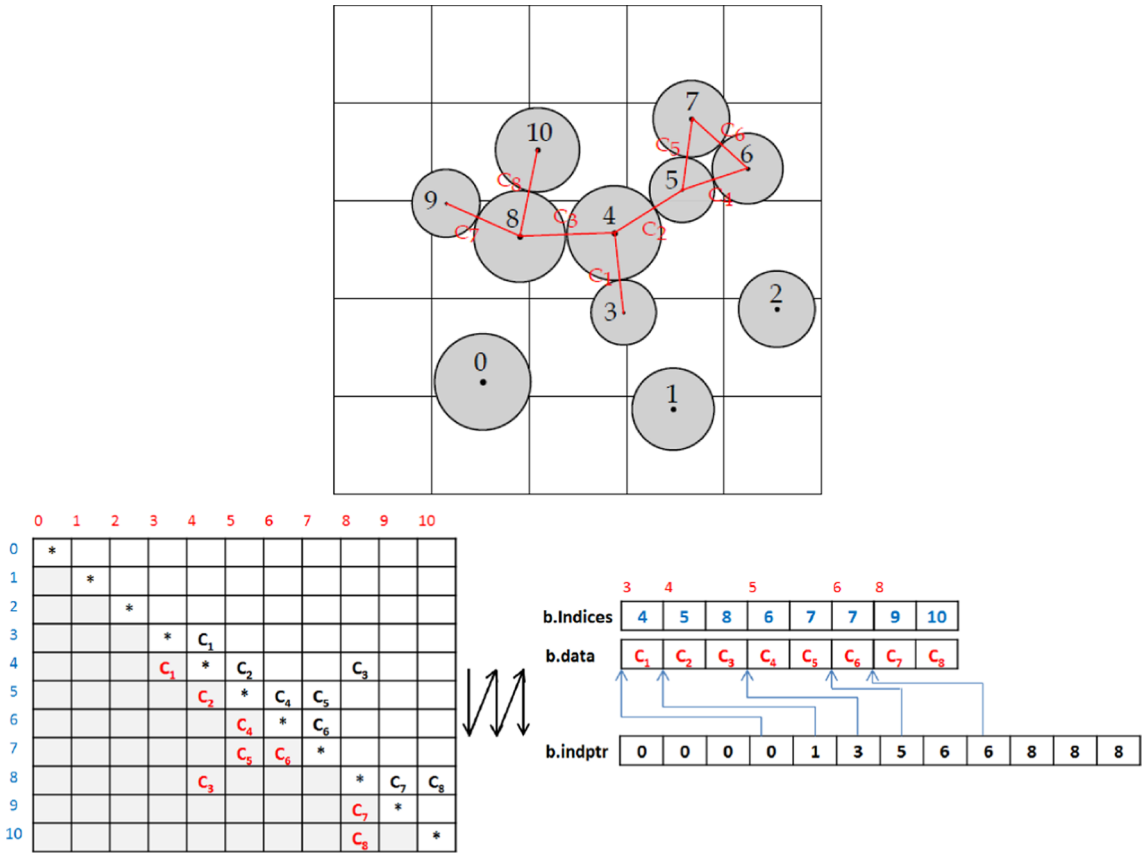

Fig. 8. Upper figure: Contact and bond detection for a granular sample with 11 particles. The cohesive bonds are displayed in red and labelled C_1 to C_8. Lower figure on the left: Symmetric sparse bond matrix corresponding to the numbering and bonds shown in the upper figure. Lower figure on the right: Corresponding arrays using the CSC storage format for sparse matrices. (For interpretation of the references to colour in this figure legend, the reader is referred to the web version of this article.)

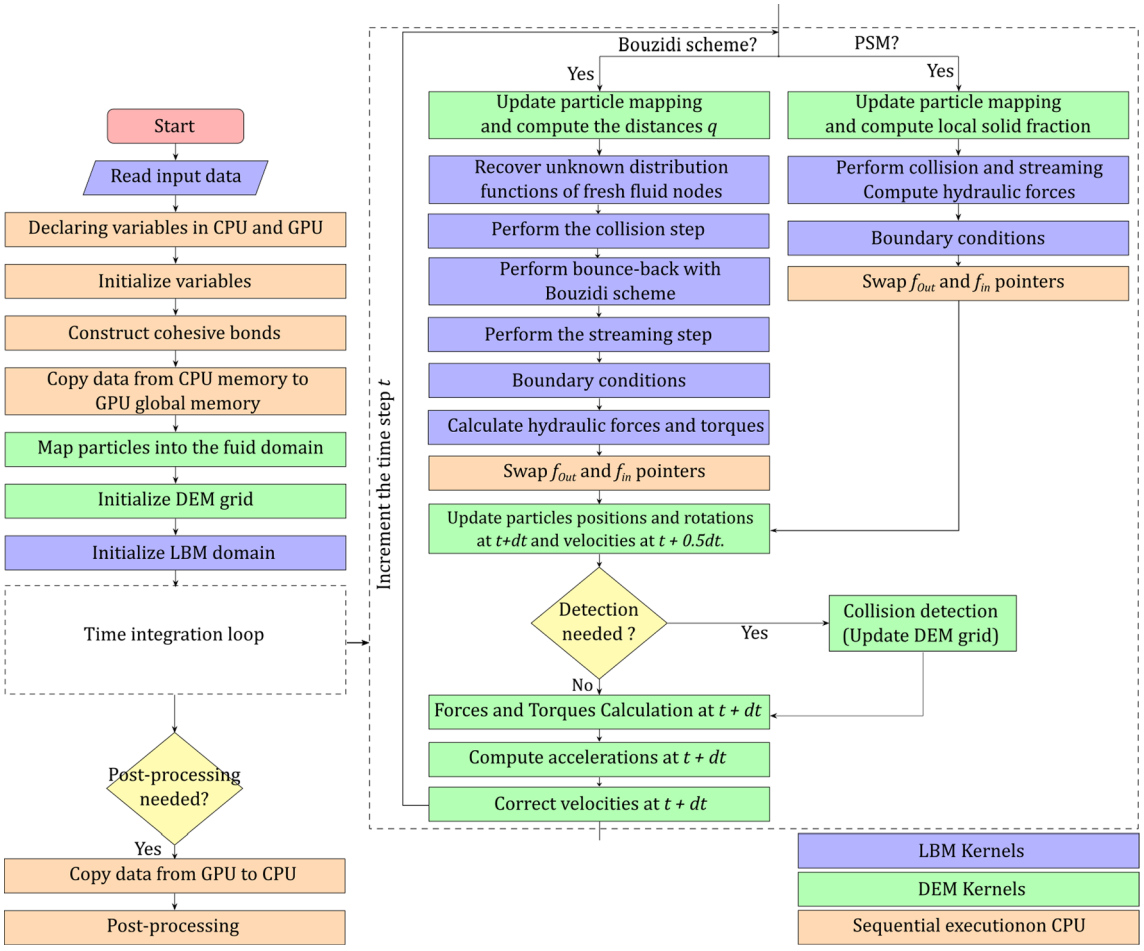

Fig. 9. Flowchart of general GPU implementation of the micromechanical simulation model featuring both alternative coupling schemes in the frame of the momentum-exchange (Bouzidi) and partial saturation method (PSM).

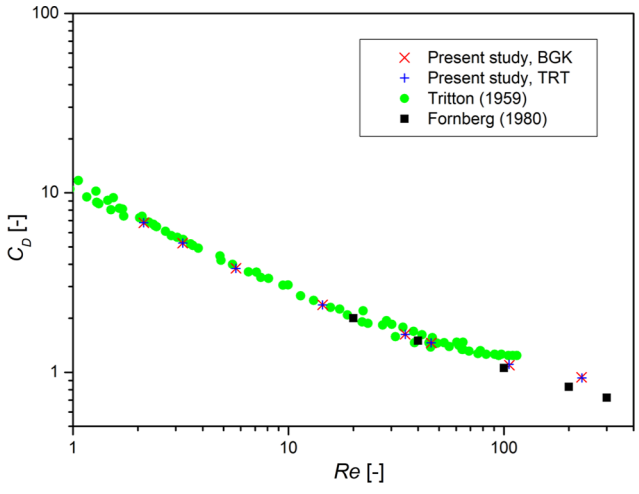

Fig. 10. Drag coefficient C_D as a function of the particle's Reynolds number Re for a single particle settling in a fluid. Simulated results depicted with red and blue cross markers. Experimental results from [92] in green solid circles and numerical results from [94] in solid square markers. (For interpretation of the references to colour in this figure legend, the reader is referred to the web version of this article.)

$$C_D = \frac{\pi(\rho_s - \rho_f)gD}{2\rho_f v_p^2} \tag{49}$$

where the particle diameter is D = 0.02 m, the ratio between the particle and fluid densities is set as $\rho_s/\rho_f = 1.01$, the gravity is set to $g = 9.81$ m/s^2, and the fluid kinematic viscosity ν is varied from 0.2 to 0.005 (in lattice units).

Fig. 10 shows the simulated results for the drag coefficient C_D versus particle Reynolds number Re using the BGK and TRT collision models respectively, the latter implemented with a magic number $\Lambda = 1/4$. For comparison, the figure also shows the experimental results of a fluid flow past a circular cylinder obtained by Tritton [92]. The good agreement with the experimental results appears to hold up to the transition from laminar to turbulent conditions, while for larger Reynolds number ($Re > 100$) it may be necessary to introduce a turbulence model (e.g. a LES scheme as in [93]). A nice agreement can also be observed by comparison with several other numerical studies such as [94] (see also [33] and references therein).

It is also remarkable that the results for both collision models are almost identical with respect to C_D. However, the simulation with the BGK collision model shows some slight spurious fluctuations in the pressure field around the particle when the fluid's kinematic viscosity is low (see Fig. 11-left) which can be avoided by using the TRT collision model (see Fig. 11-right).

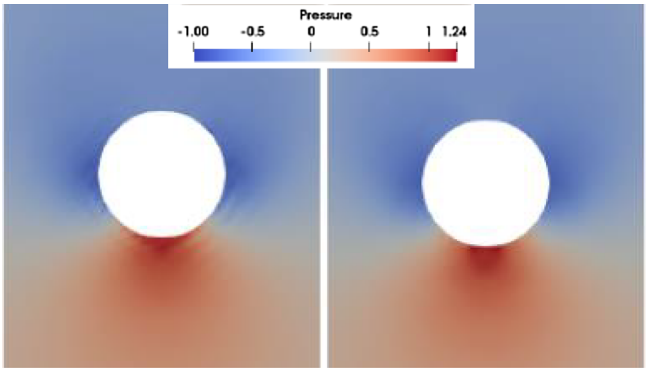

Fig. 11. Simulated results of pressure field for a kinematic viscosity $\nu = 0.025$ in lattice units. Left: Simulation with BGK collision model; Right: Simulation with the TRT collision model.

The second validation test is the sedimentation of two solid particles ($D = 0.2$ cm and density $\rho_s = 1010$ kg/m^3) in a fluid channel (channel width = 2 cm and height = 8 cm). The lattice unit size is kept here equal to D/20. Initially, both particles P1 and P2 are located at the central axis of the channel at a height of 7.2 cm and 6.8 cm respectively, while the particle P1 is laterally offset from the central axis by a single lattice step to enforce a slight asymmetry. The density and kinematic viscosity of the fluid are set here to $\rho_f = 1000$ kg/m^3 and $\nu = 1 \times 10^{-6}$ m^2/s, respectively. For the solid contacts, the normal stiffness is chosen as $k_n = 1.1 \times 10^5$ N/m, while the friction coefficient is set to zero ($\mu = 0$).

In this case, the grid size is set to $N_x \times N_y = 201 \times 801$ and the relaxation time is fixed at $\tau = 0.65$ with a corresponding time-step of $\Delta t = 5 \times 10^{-4}$ s. Once again, bounce-back (non-slip) boundary conditions are enforced at the lateral and lower walls, while the upper boundary is considered as an outlet with zero pressure. Fig. 12 shows the fluid velocity field at three different time stations of the simulation.

Fig. 13 depicts the evolution of the transverse and longitudinal coordinates of the two particles over time. These results can be compared to the so-called DKT trajectories (drafting-kissing-tumbling) presented in [95] showing a reasonable agreement both qualitative and quantitatively.

The algorithms have also been validated by means of further classical benchmark tests (e.g. the steady plane Poiseuille-flow, the lid-driven cavity and the flow past a cylinder) [33] as well as for several specific forms of complex flow configurations (laminar free jet, impinging jet on a solid smooth surface and on a fixed granular surface) for which theoretical predictions are available (see e.g. [52] and references therein). These two references also provide further qualitative comparisons of the model to real physical experiments, where the latter reference even reaches a quantitative agreement with the experimental data on the erosion thresholds for the immersed cohesionless samples. Further comparisons to physical observations for real engineering problems (e.g. installation of a suction bucket foundation) will be carried out soon in the frame of the on-going joint research project COMET (a French-German public cooperation project due to last until 2022, see details in the acknowledgements) and will be published in due course.

4. Applications and performance

Let us now examine some exemplary applications in the fields of soil erosion and geotechnical profile driving to illustrate roughly the range of possibilities provided by the micromechanical analyses with the proposed techniques. These are then followed by a discussion on the parallel performance of the presented approach.

4.1. Jet and shear erosion of immersed cohesive soil samples

The analysis of the soil erosion mechanisms under an impinging jet is a very illustrative example of a complex scenario of solid-fluid interaction where the micromechanical simulation can provide useful and detailed insights that would be hardly available by other means. This scenario has become quite relevant e.g. for the erodibility assessment of earthen hydraulic civil constructions such as earth-dams and levees. In this context, the Jet Erosion Test (JET) has gained broad acceptance due to the relative simplicity of the experimental setup and the existence of portable JET devices for the assessment *in situ* [9].

In such cases, the engineering practice usually adopts simplified assumptions concerning the hydrodynamic conditions at the jet impingement in order to derive the erodibility parameters. On the other hand, pure CFD approaches modelling an impinging jet with erosion are currently still rare due to the extreme difficulties involved in such analyses and their necessity of an assumed erosion law [96,97]. In this sense, the approach proposed here permits not only to examine the pertinence of such assumptions [52], but also to investigate the onset of erosion from a topological point of view or to assess the dependence of the critical fluid velocity for the initiation of erosion on the soil material properties such as the mean particle size or the intergranular cohesion [98,99].

As a first example, let us consider the case of a fluid jet with prescribed inflow velocity at the injection nozzle (nozzle diameter b) impinging on a fixed granular surface perpendicular to the jet's axis and located at a distance H from the nozzle (see Fig. 14). Here, the geometrical, material and rheological parameters of the model, which are summarized in Table 1, have been chosen arbitrarily either for convenience (comparison with previous experimental results [100]) or based on usual values from the literature (see e.g. [68]). The hydrodynamic conditions correspond here to an inertial laminar flow regime (i.e. transitional from laminar to turbulent conditions), with jet's Reynolds number in the range of $Re_j \sim 60$ to 160. In this case the MRT collision model was used with the relaxation parameters $s_1 = 1.63$; $s_2 = 1.14$; $s_4 = s_6 = 1.92$ and $s_7 = s_8 = 1/\tau$ as specified previously in Section 2.1.1.

The macroscopic profiles of fluid velocity, pressure and shear stress at the soil surface naturally integrate the irregularities of the granular assembly while showing the typical stagnation point of fluid velocity and its complementary maximum of fluid pressure (Fig. 15). On the other hand, the micromechanical hydraulic forces at the surface (integrated specifically on each solid grain) appear to reflect the fact that the maxima of shear stress and pressure *gradient* are actually located right on the spots of the most prominent grains (the most exposed ones) within the relevant impingement area (approximately in the range $[-H, H]$ of radial distance from the jet's axis). Such micro-scale variables appear therefore very suitable to describe the topology of erosion, at least at its onset.

Upon release of the fixed granular surface, the large pressure gradients and shear stresses induced by the jet flow lead to a general mobilization of the solid grains at the impingement area and the appearance of a scoured crater. In the presence of cohesive forces between particles, the erosion kinetics becomes slower (see e.g. the results for different strengths of the cohesive bonds and a jet velocity of 1.5 m/s in Fig. 15 left), where the eroded grains can be detached either as single particles or in multi-grain clusters preserving a number of internal bonds. The quantification of the erosion kinetics relies here on a distinction between eroded and non-eroded particles based on the grains' kinetic energy. In this case, an energy threshold of 2×10^{-4} Joules appears to discriminate well the particles at the erosion front, although this magnitude is very likely to depend on other model parameters such as the grain and cluster sizes (a typical energy can be derived e.g. from the settling velocity with the estimate of C_d from previous analysis). In

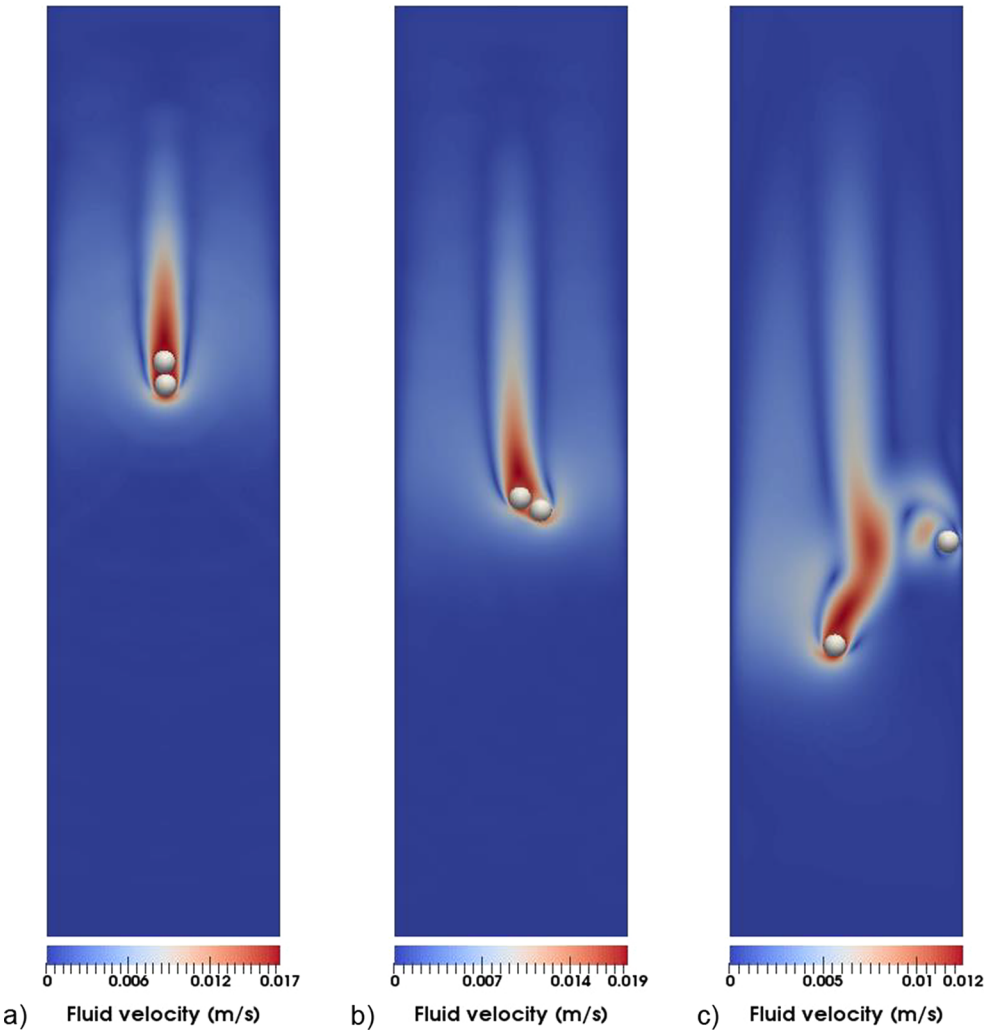

Fig. 12. Snapshots of the fluid velocity field during the settling of two immersed particles at three arbitrary time-stations showing a DKT-pattern (draft-kiss-tumble). (a) Simulated time t = 1.8 s; (b) t = 2.5 s; (c) t = 3.5 s.

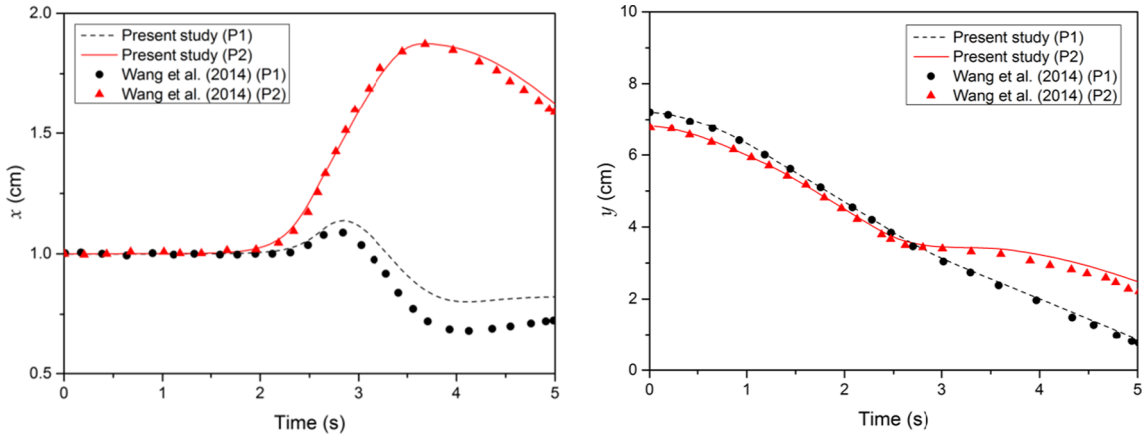

Fig. 13. Trajectories of two immersed settling particles: (left) transverse coordinates x; (right) longitudinal coordinates y. The numerical results of Wang and coworkers [95] are shown in solid markers.

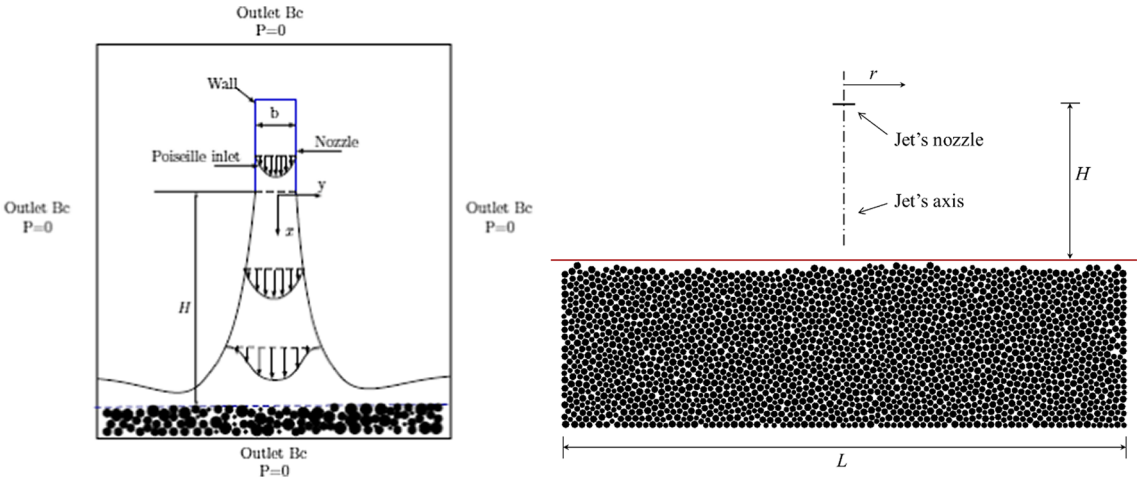

Fig. 14. Geometrical and boundary conditions for a study case of jet erosion on a granular sample. The red line indicates the adopted horizon used for deriving the surface profiles of hydrodynamic quantities. (For interpretation of the references to colour in this figure legend, the reader is referred to the web version of this article.)

Table 1
Geometrical, material and model parameters used for the simulation of jet soil erosion.

Solid phase		Fluid phase	
Particle mean size, D_{mean}	3×10^{-3} m	Jet's distance to surface, H	7×10^{-2} m
Polydispersity, D_{max} / D_{min}	1.5	Jet's nozzle size, b	5×10^{-3} m
Length of granular sample, L	2.63×10^{-1} m	Kinematic fluid viscosity, ν	5×10^{-5} m^2/s
Height of granular sample, H_s	8×10^{-2} m	Fluid density, ρ_f	847 kg/m^3
Particle density, ρ_s	2230 kg/m^3	Lattice grid size, Δx	2.3×10^{-4} m
Normal contact stiffness, k_n	1.1×10^5 N/m	Lattice speed, c	10 m/s
Shear contact stiffness, k_s	1.1×10^5 N/m	Hydraulic radius factor, R_h	0.8
Rolling stiffness, k_r	$0.1 \times k_n$	Inlet fluid velocity range, u_j	[0.45–1.5] m/s
Friction coefficients, $\mu = 3{\cdot}\mu_r$	0.3		
Normal bond stiffness, $k_{n,b}$	$0.5 \times k_n$		
Shear bond stiffness, $k_{s,b}$	$0.2 \times k_n$		
Bond's bending stiffness, $k_{m,b}$	$2 \times 10^{-6} \times k_n$ Nm/rad		
Bond strength, $C = C_n = 2C_s$	[0–2.5] N		

this case, it appears that the critical cementation degree for the complete absence of erosion should feature a minimum bond strength somewhere between 2 and 2.5 N. The actual relationship between the bond strength C and the usual macroscopic (geotechnical) cohesion c' and friction angle φ can then be explored with simple dry loading scenarios such as the biaxial compression test (see e.g. [61]).

A second erosion scenario with multiple practical applications is the soil erosion under homogeneous shear flow conditions (the so-called Couette flow type). In this case, the fluid shear stress is kept constant (i.e. the fluid inlet boundary condition is displaced progressively following the eroded surface) and the erosion rate is estimated by the vertical displacement rate of the sample's surface. In these conditions, the constant shear stress imposed by the fluid on the soil surface can be estimated as

$$\tau = \rho_f \nu \frac{U_0}{e_0} \tag{50}$$

where U_0 is the imposed shear velocity at the upper boundary and e_0 is the distance between this boundary and the sample surface (see Fig. 16). The model parameters used in this case are summarized in Table 2.

The rest of boundary conditions used in this case are the outlet pressure ($P_{out} = 0$ Pa) and the fixed grains applied at the rest of boundaries of the fluid and solid domains respectively (the "fixed" particles located at the upper limit of the lateral boundaries are let to be eroded following the evolution of fluid film thickness over time). The entrained particles, i.e. the grains with a kinetic energy above the critical threshold and with no solid contacts or bonds whatsoever, are then classified as eroded and removed from the simulation. In this respect, the use of the TRT collision model combined with PSM presents several advantages for this particular case, since the PSM collision step is performed also inside the particle's nodes, which permits the removal of the eroded grains from the system without significant changes to the algorithms. The consequent slight perturbations of the velocity and pressure fields derived from the grain's removal appear to bear no influence on the simulations and tend to be very short-lived, since they actually escape the system once they reach the outlet boundaries. Furthermore, the TRT scheme provides a smooth pressure field around the particles as already shown in the validation section.

Fig. 17 depicts the typical evolution of the system, where the vertical position of the erosion front (i.e. $e(t)$-e_0) is displaced at a roughly constant rate $\dot{\varepsilon}$ (Fig. 18 left). By repeating the analysis for different prescribed values of the fluid shear stress, it is straightforward to derive the classical macroscopic erodibility parameters, i.e. the kinetic modulus k_d and the critical shear stress τ_c as defined in the following manner [101,102] from a plot of the erosion rate versus shear stress:

$$\dot{\varepsilon} = \begin{cases} k_d(\tau - \tau_c) & if \tau > \tau_c \\ 0 & otherwise \end{cases} \tag{51}$$

However, when the simulations are performed with the basic cohesion scheme only (no damage model), the flow is unable to induce any surface erosion for the low shear stress range (here for shear stresses below ~150 Pa and a cohesive bond strength of $C = 3N$). In such cases, the sample may reach a new equilibrium state (in some

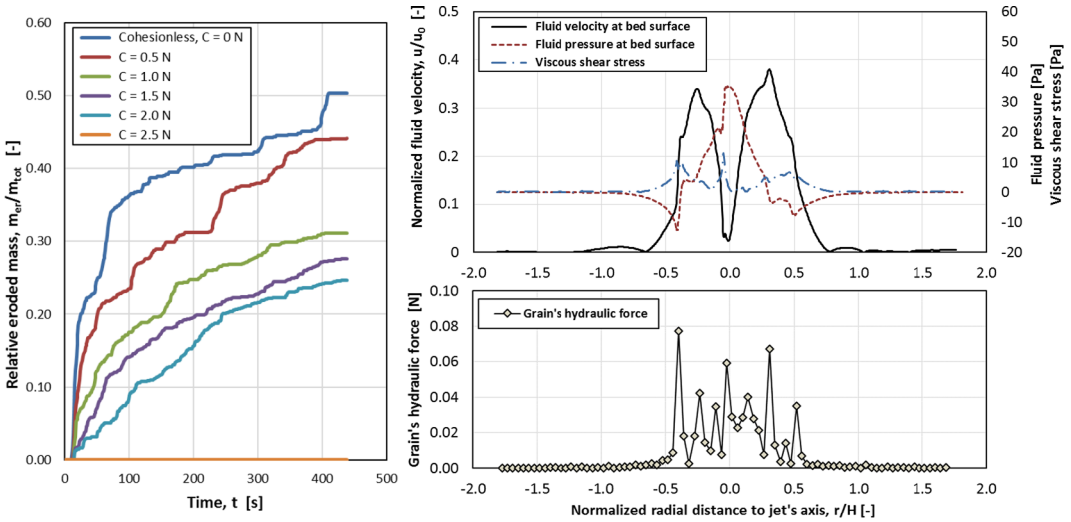

Fig. 15. Jet erosion of a cohesive granular sample. Left: Evolution of the relative eroded mass (ratio of eroded particles to the total mass of the sample) for different degrees of intergranular cohesion and a jet inflow velocity of 1.5 m/s [98]; Right: Topology of the macroscopic (above) and microscopic (below) descriptors of the hydrodynamic conditions at the jet impingement area on the surface of the fixed granular sample [99].

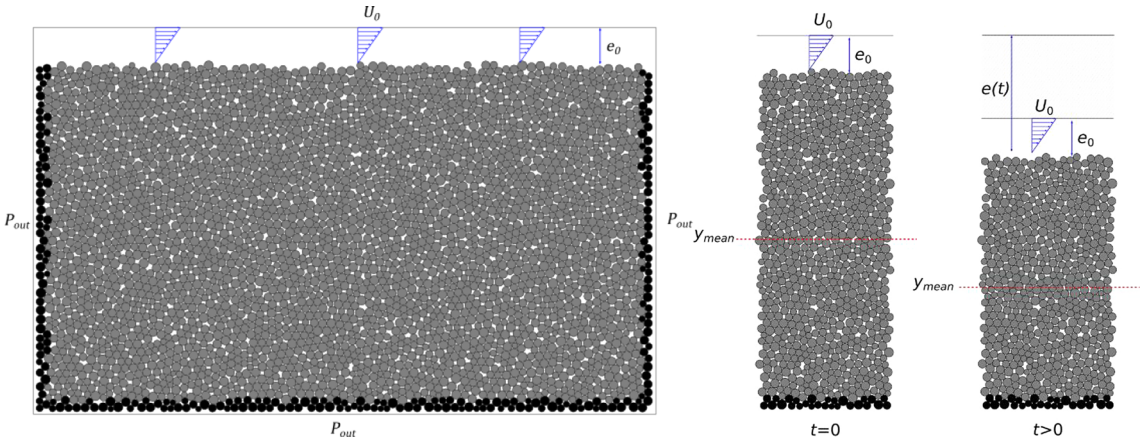

Fig. 16. Geometrical and boundary conditions for the analysis of a shear flow erosion case on a cohesive granular sample.

Table 2
Geometrical, material and model parameters used for the simulation of shear flow erosion.

Solid phase		Fluid phase	
Particle mean size, D_{mean}	3×10^{-3} m	Kinematic fluid viscosity, ν	2×10^{-4} m^2/s
Polydispersity, D_{max} / D_{min}	1.5	Fluid density, ρ_f	1000 kg/m^3
Length of granular sample, L	2.4×10^{-1} m	Lattice grid size, Δx	2.4×10^{-4} m
Height of granular sample, H_s	1.54×10^{-1} m	Lattice speed, c	[50–100] m/s
Particle density, ρ_s	2500 kg/m^3	Hydraulic radius factor, R_h	0.8
Normal contact stiffness, k_n	1.1×10^5 N/m	Prescribed shear fluid velocity, U_0	[1–10] m/s
Shear contact stiffness, k_s	1.1×10^5 N/m	BC's offset from surface, e_0	5×10^{-3} m
Rolling stiffness, k_r	$0.1 \times k_n$	Outlet pressure, P_{out}	0 Pa
Friction coefficients, $\mu = 3{\cdot}\mu_r$	0.2		
Normal bond stiffness, $k_{n,b}$	$0.5 \times k_n$		
Shear bond stiffness, $k_{s,b}$	$0.2 \times k_n$		
Bond's bending stiffness, $k_{m,b}$	$2 \times 10^{-6} \times k_n$ Nm/rad		
Bond strength, $C = C_n = 2C_s = (4/D_{mean})M_b$	3 N		

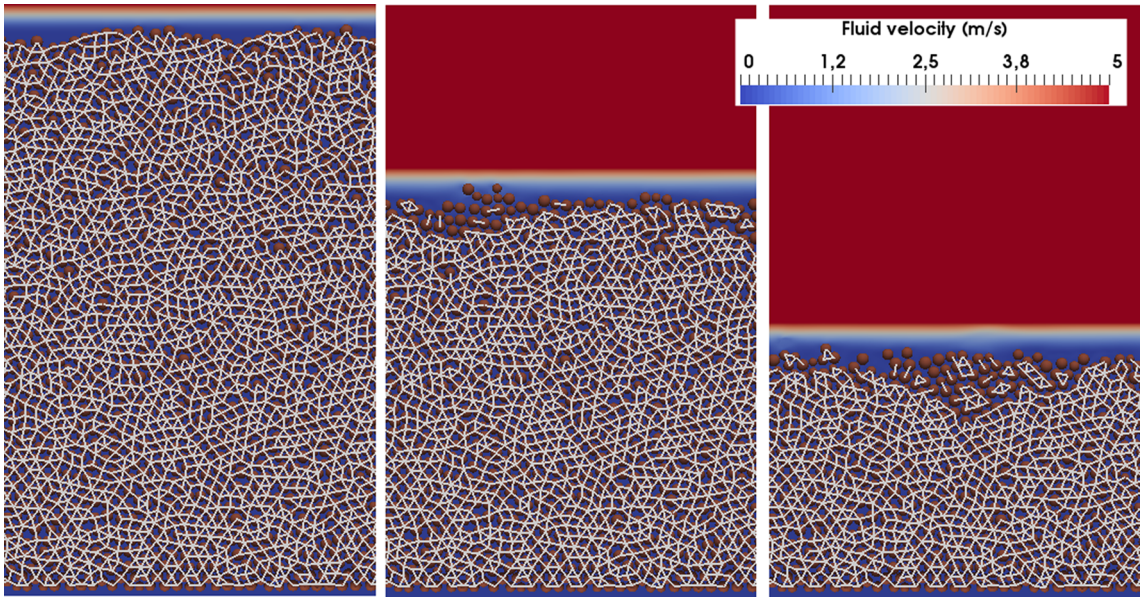

Fig. 17. Snapshots of the evolution of the erosion by shear fluid flow at three district times and part of the simulated domain is shown. The fluid velocity field is shown as gradient colour (from blue, 0 m/s to red, 5 m/s). The cohesive bond network is coloured in white, while the particles are coloured in red. No information about the cohesive bond nor the particles are shown. (For interpretation of the references to colour in this figure legend, the reader is referred to the web version of this article.)

cases involving the appearance of cracks in the bonded network of particles) that can accommodate the superficial flow stresses without further evolution. This deficiency can be mended by the inclusion of the transient damage scheme introduced in Section 2.2.3 which prevents the quasi-instantaneous opening of the sample fractures if the value for the characteristic damage time η is chosen small enough. This addition of damage extends significantly the simulation possibilities and permits to model the surface erosion in the lower range of shear stresses. A linear fitting of the results with the damage model suggests in this case a soil erodibility of around $k_d = 1.34{\cdot}10^{-4}$ $m^3/N{\cdot}s$ and $\tau_c = 33$ Pa.

As an illustration of the micromechanical investigations that can be conducted, the particular forms of solid debonding taking place during the erosion process can be conveniently analysed with a ternary plot of the failure criterion, i.e. $(F_n/C_n) + (F_s/C_s)^2 + (M/M_b)^2 = 1$, where each debonding event is represented by a point inside an equilateral triangle, accounting for the respective contribution of the traction, shear and bending solicitations, as shown in Fig. 19. In this particular case, the results appear to suggest that the most efficient forms of debonding involve either pure traction (i.e. (F_n/C_n) 1) or a combination of shear and bending solicitations with low levels of tensile forces, in the range of (F_n/C_n) $[0.3 - 0.4]$. Furthermore, the micromechanical analysis also seems to indicate a preferential debonding direction during the erosion, in this case around 60° and roughly along the main direction of tensile efforts.

All these extents are of course greatly dependent on the particular flow conditions of the simulation and the chosen material behaviour, but they already appear as a promising line of work for the design of erosion-resistant materials and the general assessment of erosion countermeasures.

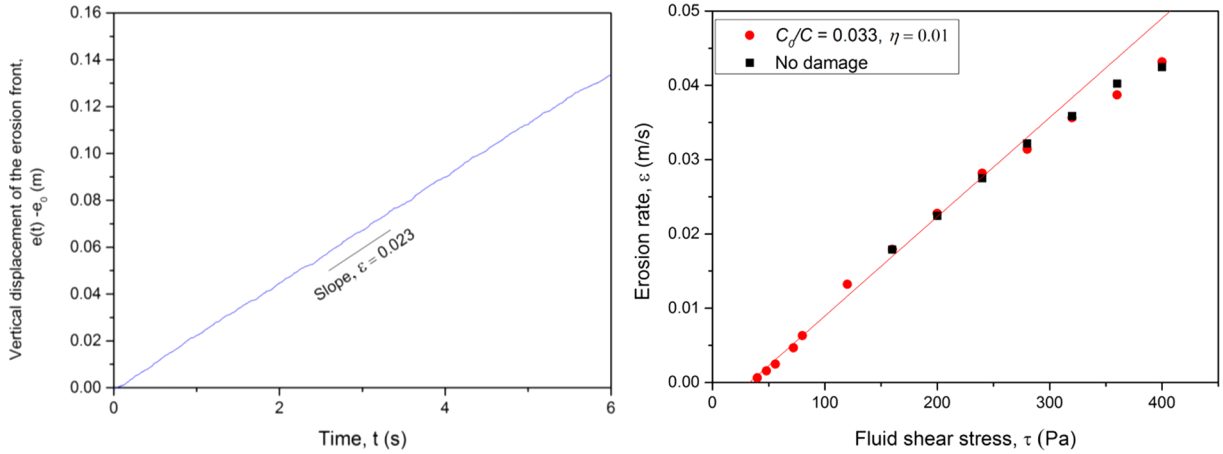

Fig. 18. Soil erosion under homogeneous shear flow conditions. Left: Evolution of the erosion front with time for a cohesive bond strength of $C = 3N$ (basic cohesion scheme without damage model) and a fluid flow involving $\nu = 2{\cdot}10^{-4}$ m^2/s, $U_0 = 5$ m/s and $e_0 = 5$ mm. Right: Variation of erosion rate ε with the prescribed fluid shear stress τ upon consideration of transient damage (damage threshold $C_0 = 0.033{\cdot}C$ and characteristic time $\eta = 0.01$). The solid line represents a linear fit of the damage data (red points) in the stress range up to 300 Pa. (For interpretation of the references to colour in this figure legend, the reader is referred to the web version of this article.)

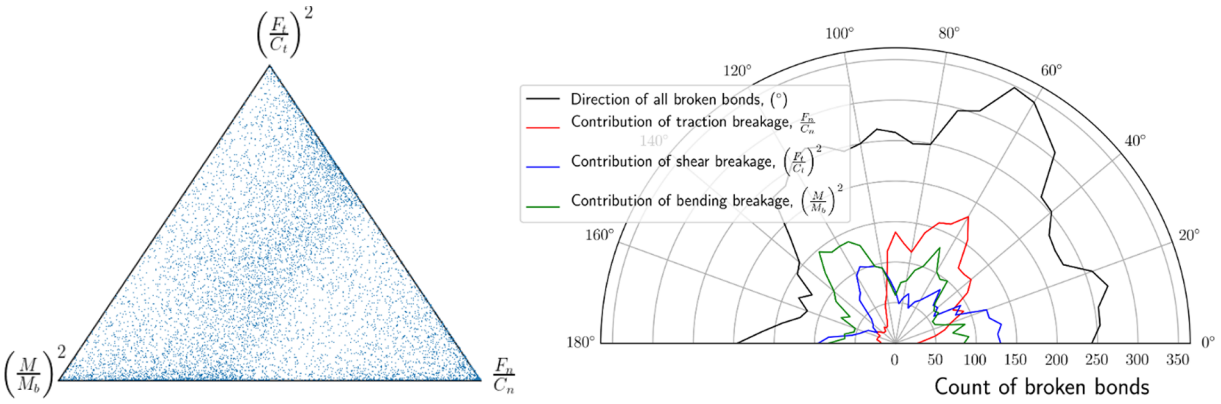

Fig. 19. Micromechanical features of the simulated shear flow erosion. Left: Ternary representation of bond failure conditions involving $\nu = 2{\cdot}10^{-4}$ m²/s, $U_0 = 5$ m/s and $e_0 = 5$ mm. Right: Angular distribution of cumulative solicitations for all broken cohesive bonds (8647 in total) during the shear flow erosion.

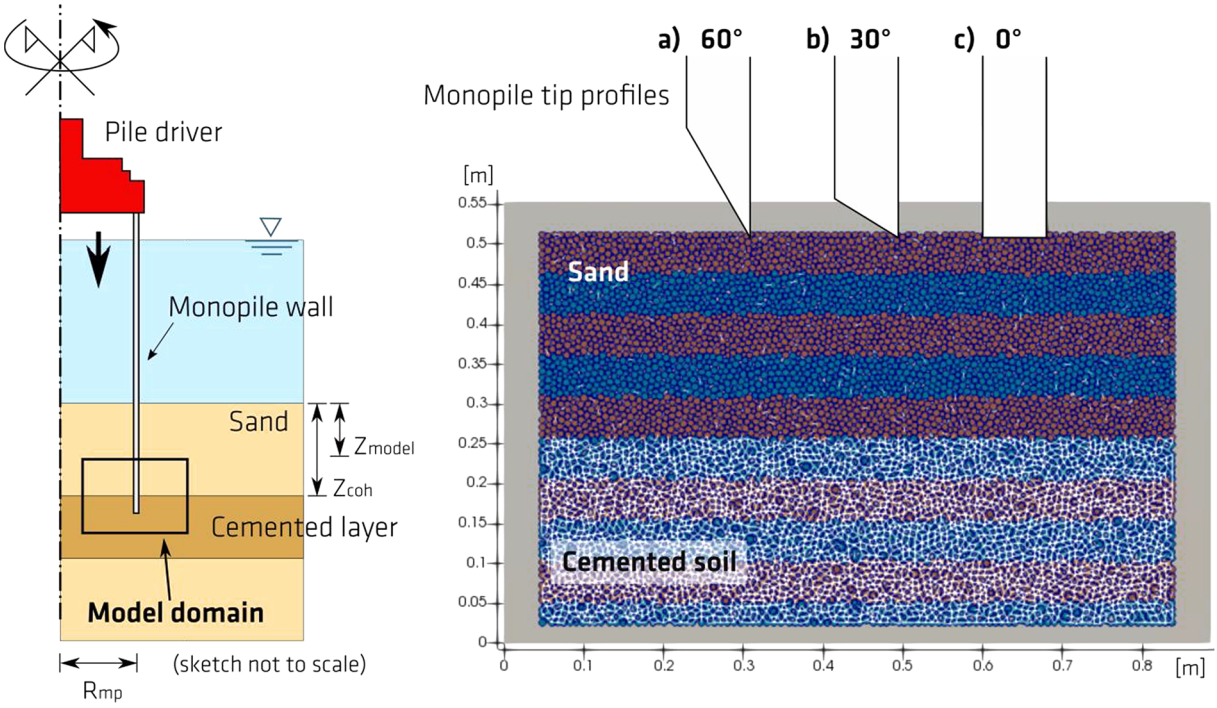

Fig. 20. Study case definition for the profile installation of an offshore monopile in fully saturated layered soil, Left: Generic situation of the study case (sketch not to scale); Right: Model domain involving the border of the cemented sand layer at half-height and three alternative shapes of the wall-tip profile. The network of intergranular cohesive bonds of the cemented sand layer is depicted in white colour; the layered colour-fill of the solid grains (pink/blue) is introduced solely for visualization purposes and does not imply a material change. (For interpretation of the references to colour in this figure legend, the reader is referred to the web version of this article.)

Table 3
Geometrical, material and model parameters for the simulations of a profile driving.

Solid granular phase		Fluid phase	
Particle mean size, D_{mean}	1×10^{-2} m	Kinematic fluid viscosity, ν	2×10^{-4} m²/s
Polydispersity, D_{max}/D_{min}	1.5	Fluid density, ρ_f	1000 kg/m³
Length of granular sample, L	8×10^{-1} m	Lattice grid size, Δx	2.3×10^{-4} m
Height of granular sample, H_s	5×10^{-2} m	Lattice speed, c	50 m/s
Particle density, ρ_s	2230 kg/m³	Hydraulic radius factor, R_h	0.78
Normal contact stiffness, k_n	1.1×10^5 N/m	Outlet pressure, P_{out}	0 Pa
Shear contact stiffness, k_s	1.1×10^5 N/m	**Study case data**	
Rolling stiffness, k_r	$0.1 \times k_n$		
Friction coefficients, $\mu = 3{\cdot}\mu_r$	0.3	Model depth, Z_{model}	4 m
Normal bond stiffness, $k_{n,b}$	$0.5 \times k_n$	Layer border depth, Z_{coh}	4.25 m
Shear bond stiffness, $k_{s,b}$	$0.2 \times k_n$	Monopile radius, R_{mp}	3 m
Bond's bending stiffness, $k_{m,b}$	$2 \times 10^{-6} \times k_n$ Nm/rad	Wall thickness, t	8×10^{-2} m
Bond strength, C	25 N	Driving speed	1×10^{-2} m/s
Effective confining pressure, σ'_0	44 kPa	Profile's tip angle	0°, 30°, 60°

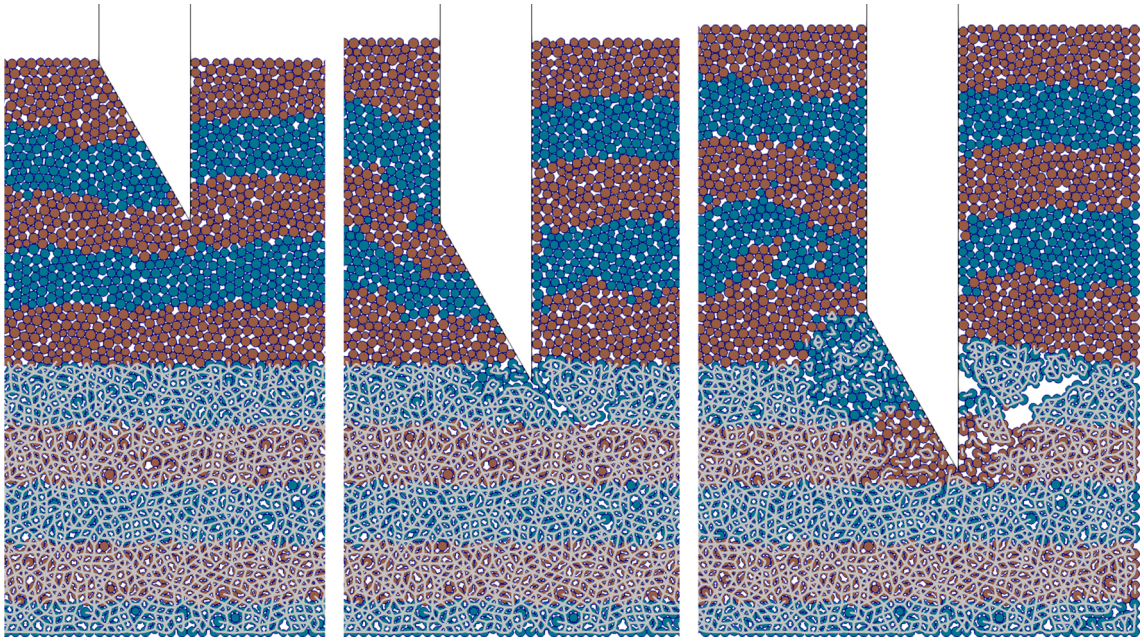

Fig. 21. Close-up sequence to the solid phase in the near-field of the pile-tip during the driving process of an offshore monopile in fully saturated layered soil, with a tip-angle of 60° inwards. Snapshots at a simulated time of t = 13 s; t = 27 s; and t = 34 s, from left to right.

4.2. Profile installation in fully saturated layered soil

The next example concerns the installation of a geotechnical profile (e.g. the steel profile of a deep foundation) into a saturated layered soil. We consider here the downwards driving of the wall-tip of an offshore monopile through two layers of soil, where the upper layer is a purely frictional granular material (e.g. cohesionless sand) and the lower layer features cohesive intergranular bonds (e.g. a siliceous sand with carbonate/calcareous cementation).

The modelled domain is assumed to rest at a depth of about 4 m below the mudline and be naturally consolidated. Therefore, the effective geostatic pressure at that depth is adopted as an approximation to the boundary conditions of the lateral and upper limits of the discrete model (constant stress boundaries). The distinct border between the two layers is assumed to be right in the middle of the domain height. For simplicity and to keep a low computational cost, the domain is here restricted to just half a metre in height and 80 cm in width, which appears to suffice for the illustrative purpose of this academic example. Concerning the monopile, it is assumed to be perfectly rigid and three different shapes of the wall-tip profile are considered, with a tip inclination of either 60°, 30° or 0° and a wall-thickness of 80 mm for all cases. For simplicity, the pile driving conditions are here assumed as quasi-static (i.e. no inertia effects) and with a penetration speed of 10 mm/s. This generic situation is illustrated in Fig. 20, while the geometrical, material and model parameters used for the simulation are summarised in Table 3.

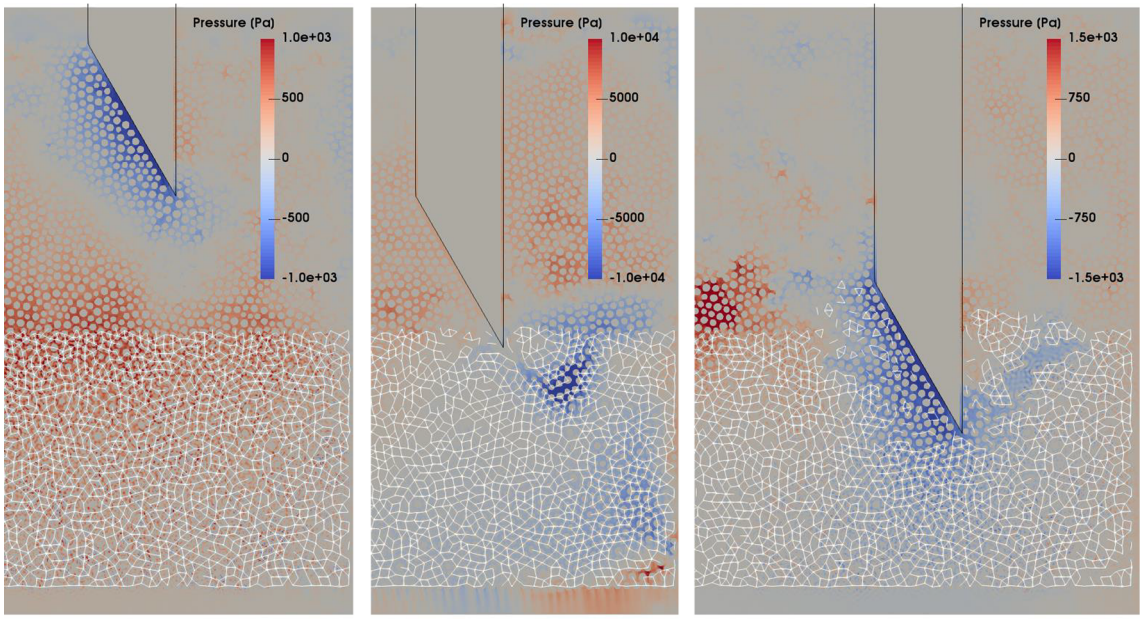

Fig. 22. Excess pressure of the fluid phase in the near-field of the pile-tip during the driving process of an offshore monopile in fully saturated layered soil, with a tip-angle of 60° inwards. Snapshots at a simulated time of t = 13 s; t = 27 s; and t = 34 s, from left to right.

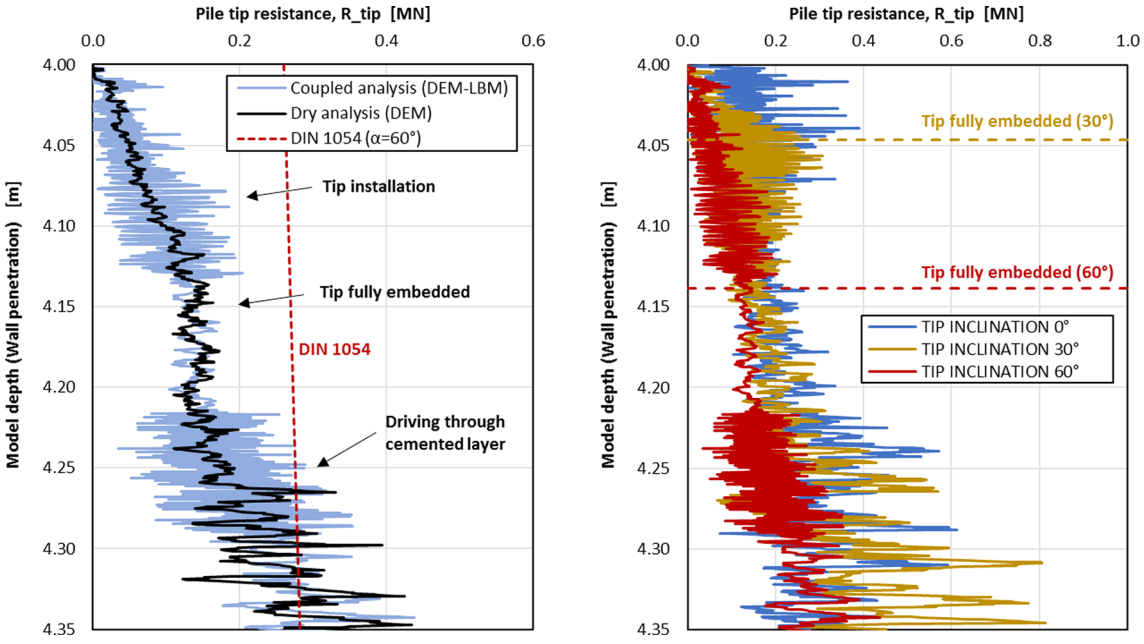

Fig. 23. Profile of vertical effective resistance experienced at the pile-tip during the driving process of an offshore monopile in fully saturated layered soil. Left: Simulated results with and without fluid coupling for a driven profile with a tip-angle of 60° inwards, as compared to a reference solution derived from the maximum bearing pressure under a strip footing with raking sole at 60° in a cohesionless soil ($\varphi = 30^{\circ}$; $c_u = 0$ Pa) according to DIN 1054 [105]. Right: Coupled results with variation of the tip-angle from 0° to 60°.

The analysis is performed in terms of effective stresses, so that the fluid pressure and confining stresses are given as excess over the hydrostatic pressure. In this sense, the boundary conditions for the fluid phase are imposed as simple pressure outlets with $P_{out} = 0$ Pa.

Fig. 21 depicts exemplarily the displacements induced in the solid granular phase at three different penetration depths in a close-up around the pile-tip. From a qualitative perspective, it is possible to appreciate the influence of the cemented layer as a stiff lower boundary for the cohesionless soil. Once the pile-tip penetrates into the bonded domain, two distinct forms of decohesion take place at either side of the pile-wall: a soil-crushing process in the inner side of the wall and beneath the inclined pile-tip, generating a Prandtl-like failure surface [103] and the mobilization of the broken material either as single grains or in small clusters of a few particles. In contrast, the failure of the cemented soil in the outer side of the wall shows a chipping process whereby large clusters of bonded material are detached and mobilized as rigid bodies.

The corresponding sequence for the excess pressure in the fluid phase is depicted in Fig. 22, generally showing a local bulb of underpressure below the tip-shoulder and moving along with the pile-tip. This marked drop in fluid pressure appears consistent with the necessary local dilatancy (i.e. volume growth) of the dense granular packing in order to accommodate the additional volume of the incoming pile-wall. Significantly, the chipping process taking place in the cemented layer leads to the creation of large voids between the clusters and thus to sudden episodes of negative pressure along the fractures.

Here it appears important to note that the results portrayed in Fig. 22 are just single instantaneous snapshots of a transient (oscillating) process involving thousands of elastic elements, so that the fluid pressure also fluctuates accordingly and it can be misleading to compare quantitatively the single snapshots (a snapshot of the instantaneous values does not allow an easy interpretation). A more detailed investigation of pore pressure (out of the scope here) may therefore be performed on the basis of time-averaged quantities to remove the fluctuations, as it is common practice in fluid mechanics, or alternatively snapshots on fluctuations (see e.g. [104]).

From a quantitative perspective, Fig. 23 portrays the installation records of effective vertical resistance experienced by the pile-tip. The relative influence of the fluid coupling is in this case illustrated by deactivating the LBM phase in a corresponding dry simulation with identical conditions in an exclusive DEM domain. The large oscillations in tip resistance of the full model appear certainly caused by local changes of pore pressure induced by the frequent grain rearrangements as the tip penetrates into the model. In this sense, a refinement of the solid particle sizes (here about 1 cm in diametre) would probably lead to reduction of the dramatic grain dislocations and smoothen out the pressure oscillations. Notably, the average resistance to driving seems to be largely comparable in both models, pointing to the large hydraulic conductivity of the model and the relative irrelevance in this case of the maximum excess of pore pressure (generally below a few kPa) as compared to the effective geostatic pressure assumed here.

As a quantitative reference and plausibility check, an approximate solution derived from the maximum bearing pressure under a simple strip footing with raking sole at 60° and strip length equal to the monopile perimeter in a cohesionless soil ($\varphi = 30^{\circ}$; $c_u = 0$ Pa) as provided by the German geotechnical standard DIN-1054 [105] is illustrated in the background of the graph. Despite the rough simplifications and the inherent differences between the two-dimensional computation and the three-dimensional solution, the computed results after full embedment of the tip appear still comparable and in the same order of magnitude as in the theoretical reference.

Concerning the influence of different pile tip geometries, the right-

Table 4
Technical specifications of the GPUs used for the performance benchmark.

	GTX 1080Ti	Tesla P100 PCIe	Tesla K80	Tesla K40m	Tesla K20xm
Architecture	Pascal	Pascal	Kepler	Kepler	Kepler
Memory [MB]	11,264	16,384	12,288	12,288	6144
CUDA cores	3584	3584	2496	2880	2688
FP32* [GFlops]	11.340	9.526	4.373	4.291	3.935
FP64** [GFlops]	1:32	1:2	1:3	1:3	1:3

* FP32: single precision (float) performance.
** FP64: double precision performance as compared to FP32.

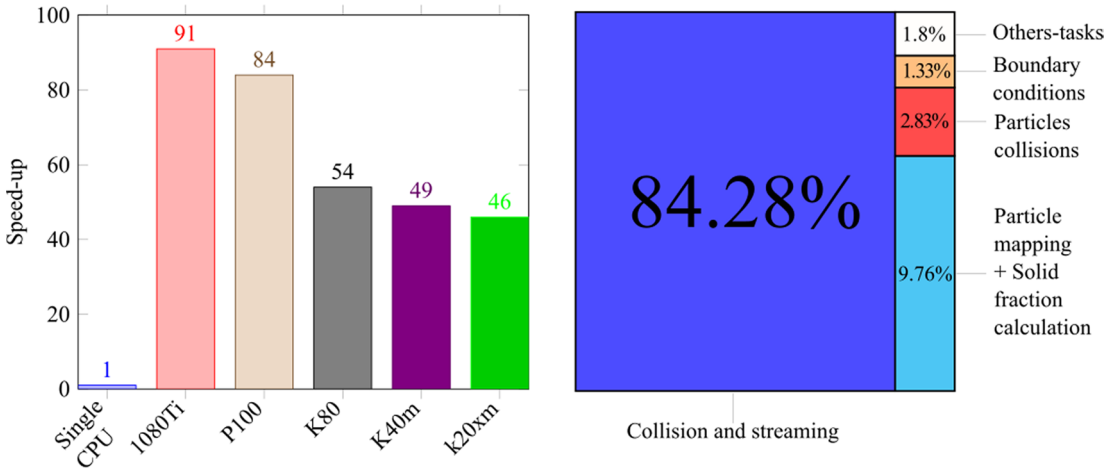

Fig. 24. Performance analyses for the parallel implementation of the code for GPUs on a JET configuration problem. Left: Speed-up factors for different commercial GPU cards as compared to the serial performance on CPU. Right: Profiling diagram of the main code kernels.

side graph in Fig. 23 shows the corresponding SRD profiles for tip inclination angles of 0°, 30° and 60°, respectively, as simulated with the fully coupled model. As expected, the adoption of the inclined profiles leads to a significant reduction of the average driving resistance, in this case up to roughly 30% reduction after full tip embedment with respect to the flat tip results.

4.3. A note on the parallel performance

The performance of the proposed parallel implementation of the code is now briefly discussed for several commercial off-the-shelf GPUs as compared to the computational speed of a serial version for CPU processing. Here it is important to keep in mind the strong dependence of the performance on the respective implementations and exercise the caution advocated by some authors (e.g. [106] or [42]). In this respect, the serial CPU version stems from a precedent development stage in the evolution of the code and is not well optimized in many aspects (e.g. the particles' neighbour search in the CPU version is performed using the classical but sub-optimal Verlet algorithm). Thus, any one-to-one comparisons of speed-ratio GPU vs CPU will generally be somewhat misleading and unfair.

For this benchmark exercise, the simulation of the Jet Erosion Test discussed previously in Section 4 is chosen as study case, with 5000 DEM particles and $N_x = 1551$; $N_y = 1001$ LBM spatial steps in the x and y directions respectively. A minimum spatial resolution of 10 lattice nodes per grain diameter is fixed for all cases. Further simulation parameters are $c = 30$ m/s and the kinematic viscosity $\nu = 4{\cdot}10^{-5}$ m^2/s, while the main technical specifications of the different GPU cards employed here are summarized Table 4. On the other hand, the serial CPU computation was performed in a DELL R820 server with 128 GB of RAM memory and an Intel Xeon E5-4617 2.90 GHz processor.

The benchmark results are summarized in Fig. 24, noting that all calculations were carried out in single precision numbers. The speed-up is here measured as the ratio of the number of time-steps computed per second in the GPUs to the reference performance of the single CPU thread. For this measurement, the monitored time-steps all involved an LBM cycle, plus a DEM step (here $N_p = 1$), plus all the output and visualization tasks specified with the given output frequency (in this case set to once every 4000 steps). Obviously, the memory transfer between GPU and CPU for the visualization steps can be reduced and the performance be enhanced by limiting the output frequency to low values. Furthermore, it also became apparent that when the TRT collision model is used, the performance slightly dropped about 1% as compared to the BGK collision model, while the inclusion of cohesion in the model did not seem to affect the overall performance in the GPU calculation.

A profiling analysis of the GPU tests is also illustrated exemplarily in the right-side graph of Fig. 24, which highlights the fact that time consumed by the DEM calculations is almost negligible as compared to the LBM expense. The LBM kernel for collision and streaming seems to consume up to about 85% of the calculation time, followed by the kernel for particle mapping and calculation of the solid fractions (about 10%). Such profiling analyses are useful to identify the potential bottlenecks to be optimized in further work.

5. Closure

This paper introduces a comprehensive micromechanical model for the analysis of geotechnical and erosion problems. The pertinence of the approach for relevant macroscopic scales and real applications is here intentionally advocated, based on the efficiency of parallel GPU computations with inexpensive and widely-available graphical cards.

On the theoretical side, the paper provides the main framework of the LBM and DEM techniques, including useful models for solid rheology, cohesive bonds and transient damage, and discusses several practical aspects for the efficiency of numerical and parallel implementations.

On the practical side, the article presents several exemplary cases of soil erosion and geotechnical profile installation in saturated soil deposits, deriving useful parameters such as the threshold cohesion for the erosion onset and the soil resistance to driving (SRD) in a layered soil profile.

To conclude, it appears important to highlight the fact that most of the modelling simplifications considered here for the sake of computational efficiency (e.g. the simplified particle shapes and large sizes,

the hydraulic conductivity of the 2D models or the obvious 2D-vs-3D spatial dimensional effects) can all be generally addressed within the proposed framework at a higher computational expense but with mere geometrical refinements and/or existing model extensions already described in the literature. In the authors' view and considering the technological developments in parallel computation of the last decade as well as the current pace of evolution in GPU/HPC units, this indicates the very large potential of micromechanical modelling for a wide range of problems in the applied sciences and engineering practice.

Declaration of Competing Interest

The authors declare that they have no known competing financial interests or personal relationships that could have appeared to influence the work reported in this paper.

Acknowledgements

The presented model has been implemented in an in-house code jointly developed by the authors and coworkers at IRSTEA and BAM with additional contributions by J. Ngoma and J.Y. Delenne and valuable exchanges with D. Chaussée (Suez Consulting Corp.). The authors gratefully acknowledge the financial support from the Région Sud, Provence-Alpes-Côte d'Azur, as well as the bi-national research grant for the ongoing COMET project, funded by the Deutsche Forschungsgemeinschaft (DFG, German Research Foundation, Projektnummer 406907912) and the Agence Nationale de la Recherche (ANR). Z. Benseghier would like to thank Vicente Cuéllar for the support and the expertise in CUDA and the DAAD organization for a short-term exchange scholarship at BAM. The authors were granted access to the HPC resources of Aix-Marseille University for this work, financed by the project Equip@Meso (ANR-10-EQPX-29-01) of the program «Investissements d'Avenir» supervised by the Agence Nationale de la Recherche.

References

[1] Mörz T, Karlik EA, Kreiter S, Kopf A. An experimental setup for fluid venting in unconsolidated sediments: new insights to fluid mechanics and structures. Sed Geol 2007;196(1–4):251–67.
[2] Lowe DR. Water escape structures in coarse-grained sediments. Sedimentology 1975;22:157–204.
[3] Betat A, Frette V, Rehberg I. Sand ripples induced by water shear flow in an annular channel. Phys Rev Lett 1999;83(1):88–91.
[4] Parteli EJR, Kroy K, Tsoar H, Andrade JS, Pöschel T. Morphodynamic modeling of aeolian dunes: review and future plans. Eur Phys J Spec Top 2014;223(11):2269–83.
[5] Baykal C, Sumer BM, Fuhrman DR, Jacobsen NG, Fredsøe J. Numerical investigation of flow and scour around a vertical circular cylinder. Philos Trans Roy Soc A: Math, Phys Eng Sci 2015;373.
[6] Chen H-H, Yang R-Y, Hwung H-H. Study of hard and soft countermeasures for scour protection of the jacket-type offshore wind turbine foundation. J Marine Sci Eng 2014;2(3):551–67.
[7] Fell R, Fry J-J. Internal erosion of dams and their foundations. London: Taylor & Francis; 2007.
[8] Bonelli S. Erosion in geomechanics applied to dams and levees. Wiley & Sons; 2013.
[9] Hanson GJ, Cook KR. Apparatus, test procedures, and analytical methods to measure soil erodibility in situ. Appl Eng Agric 2004;20(4):455.
[10] Wan CF, Fell R. Investigation of Rate of Erosion of Soils in Embankment Dams. J Geotech Geoenviron Eng 2004;130(4):373–80.
[11] Benahmed N, Bonelli S. Investigating concentrated leak erosion behaviour of cohesive soils by performing hole erosion tests. Eur J Environ Civ Eng 2012;16(1):43–58.
[12] Shafii I, Briaud JL, Chen HC, Shidlovskaya A. Relationship between soil erodibility and engineering properties. In: Procs.8th Int. Conf. on Scour and Erosion, Oxford, UK; 2016.
[13] Sumer BM, Fredsøe J. The mechanics of scour in the marine environment. World Scientific Publishing Co Pte Ltd.; 2002.
[14] Harris JM, Whitehouse R, Benson T. The time evolution of scour around offshore structures. In: Paper presented at the Proceedings of the ICE - Maritime Engineering; 2010.
[15] Matutano C, Negro V, López-Gutiérrez J-S, Esteban MD. Scour prediction and scour protections in offshore wind farms. Renewable Energy 2013;57(Supplemet C):358–65.
[16] Whitehouse RJS, Harris JM, Sutherland J, Rees J. The nature of scour development and scour protection at offshore windfarm foundations. Mar Pollut Bull 2011;62(1):73–88.
[17] De Vos L, De Rouck J, Troch P, Frigaard P. Empirical design of scour protections around monopile foundations: Part 1: Static approach. Coast Eng 2011;58(6):540–53.
[18] Stahlmann A. Numerical and experimental modeling of scour at foundation structures for offshore wind turbines. In: Procs. 23rd Int. Offshore and Polar Engineering Conference, Anchorage, Alaska, USA, June 30–July 5; 2013.
[19] Dashti S, Bray JD, Pestana JM, Riemer M, Wilson D. Mechanisms of seismically induced settlement of buildings with shallow foundations on liquefiable soil. J Geotech Geoenviron Eng 2009;136(1):151–64.
[20] Kilburn CR, Petley DN. Forecasting giant, catastrophic slope collapse: lessons from Vajont, Northern Italy. Geomorphology 2003;54(1–2):21–32.
[21] Cuéllar P, Baeßler M, Rücker W. Pore-pressure accumulation and soil softening around pile foundations for offshore wind turbines. In: Procs. 31st International Conference on Ocean, Offshore and Arctic Engineering OMAE2012, Rio de Janeiro, Brazil; 2012.
[22] Cuéllar P, Mira P, Pastor M, Fernández Merodo JA, Baeßler M, Rücker W. A numerical model for the transient analysis of offshore foundations under cyclic loading. Comput Geotech 2014;59:75–86.
[23] Esteghamatian A, Rahmani M, Wachs A. Numerical models for fluid-grains interactions: opportunities and limitations. EPJ Web Conf 2017;140:09013.
[24] Knight C, Abdol Azis MH, O'Sullivan C, van Wachem B, Dini D. Sensitivity analysis of Immersed Boundary Method simulations of fluid flow in dense polydisperse random grain packings. EPJ Web Conf 2017;140:15006.
[25] Succi S. The Lattice Boltzmann equation: for complex states of flowing matter. Oxford: Oxford University Press; 2018.
[26] Krüger T, Kusumaatmaja H, Kuzmin A, Shardt O, Silva G, Viggen EM. The Lattice Boltzmann method: principles and practice. Springer International Publishing; 2016.
[27] Rettinger C, Rüde U. A comparative study of fluid-particle coupling methods for fully resolved lattice Boltzmann simulations. Computers & Fluids 2017;154(Supplement C):74–89.
[28] Krause MJ, Klemens F, Henn T, Trunk R, Nirschl H. Particle flow simulations with homogenised lattice Boltzmann methods. Particuology 2017;34:1–13.
[29] Tomac I, Gutierrez M. Discrete element modeling of non-linear submerged particle collisions. Granular Matter 2013;15(6):759–69.
[30] Tomac I, Gutierrez M. Micromechanics of proppant agglomeration during settling in hydraulic fractures. J Petrol Explor Prod Technol 2015;5(4):417–34.
[31] Leonardi A, Cabrera M, Wittel FK, Kaitna R, Mendoza M, Wu W, Herrmann HJ. Granular-front formation in free-surface flow of concentrated suspensions. Phys Rev E 2015;92(5):052204.
[32] Tran DK, Prime N, Froiio F, Callari C, Vincens E. Numerical modelling of backward front propagation in piping erosion by DEM-LBM coupling. Eur J Environ Civ Eng 2017;21(7–8):960–87.
[33] Ngoma J, Philippe P, Bonelli S, Radjaï F, Delenne J-Y. Two-dimensional numerical simulation of chimney fluidization in a granular medium using a combination of discrete element and lattice Boltzmann methods. Phys Rev E 2018;97(5):052902.
[34] Rettinger C, Godenschwager C, Eibl S, Preclik T, Schruff T, Frings R, et al. Fully resolved simulations of dune formation in riverbeds. In: Kunkel JM, Yokota R, Balaji P, Keyes D, editors. High Performance Computing: 32nd International Conference, ISC High Performance 2017. Frankfurt: Germany, June; 2017. p. 18–22.
[35] Bartuschat D, Fischermeier E, Gustavsson K, Rüde U. Two computational models for simulating the tumbling motion of elongated particles in fluids. Computers & Fluids 2016;127(Supplement C):17–35.
[36] Fu Xiaowu, Yao Zhaohui, Zhang Xiwen. Numerical simulation of polygonal particles moving in incompressible viscous fluids. Particuology 2017;31(Supplement C):140–51. https://doi.org/10.1016/j.partic.2016.05.016.
[37] Yang GC, Kwok CY, Sobral YD. The role of fluid viscosity in an immersed granular collapse. EPJ Web Conf 2017;140:09037.
[38] Iglberger K, Rüde U. Massively parallel rigid body dynamics simulations. Comput Sci - Res Dev 2009;23(3):159–67.
[39] Schornbaum F, Rüde U. Massively parallel algorithms for the lattice Boltzmann method on nonuniform grids. SIAM J Sci Comput 2016;38(2):C96–126.
[40] Bauer M, Schornbaum F, Godenschwager C, Markl M, Anderl D, Köstler H, et al. A

Python extension for the massively parallel multiphysics simulation framework waLBerla. Int J Parallel Emergent Distrib Syst 2016;31(6):529–42.
[41] Bauer M, Eibl S, Godenschwager C, Kohl N, Kuron M, Rettinger C, et al. waLBerla: A block-structured high-performance framework for multiphysics simulations. arXiv preprint arXiv:1909.13772; 2019.
[42] Rakotonirina AD, Wachs A. Grains3D, a flexible DEM approach for particles of arbitrary convex shape - Part II: Parallel implementation and scalable performance. Powder Technol 2018;324:18–35.
[43] Feichtinger C, Habich J, Köstler H, Rüde U, Aoki T. Performance modeling and analysis of heterogeneous lattice Boltzmann simulations on CPU–GPU clusters. Parallel Computing 2015;46(Supplement C):1–13.
[44] Govender N, Wilke D, Pizette P, Khinast J. BlazeDEM3D-GPU A Large Scale DEM simulation code for GPUs. EPJ Web Conf 2017;140:06025.
[45] Qian YH, D'Humières D, Lallemand P. Lattice BGK models for Navier-stokes equation. Europhys Lett (EPL) 1992;17(6):479–84.
[46] Bhatnagar PL, Gross EP, Krook M. A model for collision processes in gases. I. Small amplitude processes in charged and neutral one-component systems. Phys Rev 1954;94(3):511–25.
[47] Lallemand P, Luo L-S. Theory of the lattice Boltzmann method: Dispersion, dissipation, isotropy, Galilean invariance, and stability. Phys Rev E 2000;61(6):6546–62.
[48] Ginzburg I, Verhaeghe F, d'Humieres D. Study of simple hydrodynamic solutions with the two-relaxation-times lattice Boltzmann scheme. Comm Comput Phys 2008;3(3):519–81.
[49] Ginzburg I, d'Humières D, Kuzmin A. Optimal stability of advection-diffusion lattice boltzmann models with two relaxation times for positive/negative equilibrium. J Stat Phys 2010;139(6):1090–143.
[50] Zou Q, He X. On pressure and velocity boundary conditions for the lattice Boltzmann BGK model. Phys Fluids 1997;9(6):1591–8.
[51] Latt J, Chopard B, Malaspinas O, Deville M, Michler A. Straight velocity boundaries in the lattice Boltzmann method. Phys Rev E 2008;77(5):056703.
[52] Benseghier Z, Cuéllar P, Luu L-H, Delenne J-Y, Bonelli S, Philippe P. Relevance of the free jet model for the soil erosion by impinging jets. J Hydraul Eng 2019;146(1):04019047.
[53] Wang M, Feng YT, Wang Y, Zhao TT. Periodic boundary conditions of discrete element method-lattice Boltzmann method for fluid-particle coupling. Granular Matter 2017;19(3):43.
[54] Azéma E, Estrada N, Preechawuttipong I, Delenne J-Y, Radjai F. Systematic description of the effect of particle shape on the strength properties of granular media. EPJ Web Conf 2017;140:06026.
[55] Matuttis H-G, Nawa M, Krengel D. Stress-Strain diagrams for non-convex particles. EPJ Web Conf 2017;140:06005.
[56] Schinner A, Matuttis H-G. Molecular dynamics simulation of cohesive granular materials, Berlin, Heidelberg; 2000.
[57] Kadau D, Bartels G, Brendel L, Wolf DE. Contact dynamics simulations of compacting cohesive granular systems. Comput Phys Commun 2002;147(1):190–3.
[58] Atkinson Barry Kean, Meredith Philip George. The theory of subcritical crack growth with applications to minerals and rocks. Fracture Mechanics of Rock Elsevier; 1987. p. 111–66. https://doi.org/10.1016/B978-0-12-066266-1.50009-0.
[59] Oldecop LA, Alonso EE. Theoretical investigation of the time-dependent behaviour of rockfill. Géotechnique 2007;57(3):289–301.
[60] Tran T-H, Vénier R, Cambou B. Discrete modelling of rock-ageing in rockfill dams. Comput Geotech 2009;36(1):264–75.
[61] Delenne J-Y, El Youssoufi MS, Cherblanc F, Bénet J-C. Mechanical behaviour and failure of cohesive granular materials. Int J Numer Anal Meth Geomech 2004;28(15):1577–94.
[62] Silvani C, Bonelli S, Désoyer T. Fracture of rigid solids: a discrete approach based on a damaging interface modelling. Comptes Rendus de Mécanique, no 2007;335:455–60.
[63] Silvani C, Désoyer T, Bonelli S. Discrete modelling of time-dependent rockfill behaviour. Int J Numer Anal Meth Geomech 2009;33:665–85.
[64] Cundall PA, Strack ODL. A discrete numerical model for granular assemblies. Géotechnique 1979;29(1):47–65.
[65] Radjai F, Dubois F. Discrete-element modeling of granular materials. Wiley-Iste; 2011.
[66] Luding S, Rivas Abud N, Weinhart T. From soft and hard particle simulations to continuum theory for granular flows. In: Luding S, Combe G, Taghizadeh K, editors. ALERT Doctoral School 2017: Discrete Element Modeling. Alliance of Laboratories in Europe for Education, Research and Technology; 2017. p. 3–42.
[67] Swope WC, Andersen HC, Berens PH, Wilson KR. A computer simulation method for the calculation of equilibrium constants for the formation of physical clusters of molecules: application to small water clusters. J Chem Phys 1982;76(1):637–49.
[68] Luding S. Cohesive, frictional powders: contact models for tension. Granular Matter 2008;10(4):235.
[69] Coetzee CJ. Review: Calibration of the discrete element method. Powder Technol 2017;310:104–42.
[70] Otsubo M, O'Sullivan C, Shire T. Empirical assessment of the critical time increment in explicit particulate discrete element method simulations. Comput Geotech 2017;86:67–79.
[71] Collins BD, Sitar N. Geotechnical properties of cemented sands in steep slopes. J Geotech Geoenviron Eng 2009;135(10):1359–66.
[72] Potyondy DO, Cundall PA. A bonded-particle model for rock. Int J Rock Mech Min Sci 2004;41(8):1329–64.
[73] Tomac I, Gutierrez M. Coupled hydro-thermo-mechanical modeling of hydraulic fracturing in quasi-brittle rocks using BPM-DEM. J Rock Mech Geotech Eng 2017;9(1):92–104.
[74] Nase ST, Vargas WL, Abatan AA, McCarthy JJ. Discrete characterization tools for cohesive granular material. Powder Technol 2001;116(2):214–23.
[75] Castellanos A. The relationship between attractive interparticle forces and bulk behaviour in dry and uncharged fine powders. Adv Phys 2005;54(4):263–376.
[76] Philippe P, Cuéllar P, Brunier-Coulin F, Luu L-H, Benahmed N, Bonelli S, et al. Physics of soil erosion at the microscale. EPJ Web Conf. 2017;140:08014.
[77] Aidun CK, Lu Y, Ding EJ. Direct analysis of particulate suspensions with inertia using the discrete Boltzmann equation. J Fluid Mech 1998;373:287–311.
[78] Bouzidi MH, Firdaouss M, Lallemand P. Momentum transfer of a Boltzmann-lattice fluid with boundaries. Phys Fluids 2001;13(11):3452–9.
[79] Lallemand P, Luo L-S. Lattice Boltzmann method for moving boundaries. J Comput Phys 2003;184(2):406–21.
[80] Mansouri M, El Youssoufi MS, Nicot F. Numerical simulation of the quicksand phenomenon by a 3D coupled Discrete Element - Lattice Boltzmann hydro-mechanical model. Int J Numer Anal Meth Geomech 2017;41(3):338–58.
[81] Ladd AJC. Numerical simulations of particulate suspensions via a discretized Boltzmann equation. Part 1. Theoretical foundation. J Fluid Mech 1994;271:285–309.
[82] Noble DR, Torczynski JR. A Lattice-Boltzmann method for partially saturated computational cells. Int J Mod Phys C 1998;09(08):1189–201.
[83] Cook BK, Noble DR, Williams JR. A direct simulation method for particle-fluid systems. Eng Comput 2004;21(2/3/4):151–68.
[84] Zhang P, Galindo-Torres SA, Tang H, Jin G, Scheuermann A, Li L. An efficient Discrete Element Lattice Boltzmann model for simulation of particle-fluid, particle-particle interactions. Comput Fluids 2017;147:63–71.
[85] Cui X, Li J, Chan A, Chapman D. A 2D DEM–LBM study on soil behaviour due to locally injected fluid. Particuology 2012;10(2):242–52.
[86] Boutt DF, Cook BK, McPherson BJOL, Williams JR. Direct simulation of fluid-solid mechanics in porous media using the discrete element and lattice-Boltzmann methods. J Geophys Res Solid Earth 2007;112(B10).
[87] Yu D, Mei R, Luo L-S, Shyy W. Viscous flow computations with the method of lattice Boltzmann equation. Prog Aerosp Sci 2003;39(5):329–67.
[88] Obrecht C, Kuznik F, Tourancheau B, Roux J-J. Multi-GPU implementation of the lattice Boltzmann method. Comput Math Appl 2013;65(2):252–61.
[89] Xu L, Song A, Zhang W. Scalable parallel algorithm of multiple-relaxation-time lattice Boltzmann method with large eddy simulation on multi-GPUs. Sci Prog 2018;2018:12.
[90] Molla MM, Haque MJ, Khan MAI, Saha SC. GPU accelerated multiple-relaxation-time lattice Boltzmann simulation of convective flows in a porous media. Front Mech Eng 2018;4(15).
[91] Sen S, Mittal S, Biswas G. Steady separated flow past a circular cylinder at low Reynolds numbers. J Fluid Mech 2009;620:89–119.
[92] Tritton DJ. Experiments on the flow past a circular cylinder at low Reynolds numbers. J Fluid Mech 1959;6(4):547–67.
[93] Feng YT, Han K, Owen DRJ. Coupled lattice Boltzmann method and discrete element modelling of particle transport in turbulent fluid flows: Computational issues. Int J Numer Meth Eng 2007;72(9):1111–34.
[94] Fornberg B. A numerical study of steady viscous flow past a circular cylinder. J Fluid Mech 1980;98(4):819–55.
[95] Wang L, Guo ZL, Mi JC. Drafting, kissing and tumbling process of two particles with different sizes. Comput Fluids 2014;96:20–34.
[96] Mercier F, Bonelli S, Pinettes P, Golay F, Anselmet F, Philippe P. Comparison of computational fluid dynamic simulations with experimental jet erosion tests results. J Hydraul Eng 2014;140(5).
[97] Mercier F, Golay F, Bonelli S, Anselmet F, Borghi R, Philippe P. 2D axisymmetrical numerical modelling of the erosion of a cohesive soil by a submerged turbulent impinging jet. Eur J Mech - B/Fluids 2014;45(Supplement C):36–50.
[98] Cuéllar P, Philippe P, Bonelli S, Benahmed N, Brunier-Coulin F, Ngoma J, et al. Micromechanical analysis of the surface erosion of a cohesive soil by means of a coupled LBM-DEM model. In: Procs. 4th. International Conference on Particle-based Methods PARTICLES 2015, Barcelona, Spain; 2015.
[99] Cuéllar P, Luu L-H, Philippe P, Brunier-Coulin F, Benahmed N, Bonelli S, et al. Micromechanical features of jet erosion - A numerical perspective. Procs. ICSE 2016 (8th International Conference on Scour and Erosion), Oxford, UK; 2016.
[100] Brunier-Coulin F, Cuéllar P, Philippe P. Erosion onset of a cohesionless granular medium by an immersed impinging round jet. Phys Rev Fluids 2017;2(3):034302.
[101] Partheniades E. Erosion and deposition of cohesive soils. J Hydraulics Division

1965;91(1):105–39.
[102] Ariathurai R, Arulanandan K. Erosion rates of cohesive soils. J Hydraulics Division 1978;104(2):279–83.
[103] Van Baars S. The axisymetric failure mechanism of circular shallow foundations and pile foundations in non-cohesive soils. Comput Mater Civ Eng 2017;2(1):1–15.
[104] Radjai F, Roux S. Turbulentlike fluctuations in quasistatic flow of granular media. Phys Rev Lett 2002;89(6):064302.
[105] DIN 1054: 2010-12 - Baugrund – Sicherheitsnachweise im Erd und Grundbau (2005) – Ergänzende Regelungen zu DIN EN 1997-1, (2010). DIN Deutsches Institut für Normung e.V. [In German].
[106] Shigeto Y, Sakai M. Parallel computing of discrete element method on multi-core processors. Particuology 2011;9(4):398–405.